Universidad Técnica Federico Santa María
Departamento de Ingeniería Eléctrica
Valparaíso, Chile

Weak-Grid Impact on Reserve Deliverability of DFIG-Based Wind Power Plants

Víctor Andrés Navarro García

2026

Requisito parcial para obtener el grado de:
Magíster en Ciencias de la Ingeniería Eléctrica

Profesor Guía:
Dr. Esteban Gil Sagás (UTFSM)

Valparaíso, julio de 2026.

CONSTANCIA DE VALIDACIÓN Y CONFIDENCIALIDAD DE MONOGRAFÍA A REPOSITORIO ACADÉMICO

1.- IDENTIFICACIÓN DEL TRABAJO ACADÉMICO

Tipo de monografía (marcar una opción): ☐ Memoria o trabajo de título ☒ Tesis de Postgrado

Título del trabajo:
Weak-Grid Impact on Reserve Deliverability of DFIG-Based Wind Power Plants

Nombre del candidato(a):
Víctor Andrés Navarro García

Carrera / Grado:
Magíster en Ingeniería Civil Eléctrica

Campus: Casa Central **Departamento:** Ingeniería Eléctrica

2.- VALIDACIÓN DEL PROFESOR GUÍA/DIRECTOR DE TESIS

Yo, Esteban Manuel Gil Sagas, en mi calidad de profesor(a) guía/director(a) del trabajo académico mencionado anteriormente **DEJO CONSTANCIA** que:

- He revisado esta versión del documento y corresponde a la versión final aprobada del trabajo.
- El trabajo cumple con los requisitos académicos y de formato establecidos por la institución.

3.- EVALUACIÓN DE CONFIDENCIALIDAD POR PROPIEDAD INDUSTRIAL (marcar una opción)

☒ El trabajo **NO contiene** información que amerite confidencialidad y puede ser publicado de inmediato en repositorio con acceso abierto.

☐ El trabajo **CONTIENE** información con potenciales implicancias de propiedad industrial o intelectual y requiere un periodo de confidencialidad (**embargo**) por **(marcar una opción)**:

☐ 6 meses ☐ 12 meses ☐ 2 años ☐ 3 años ☐ 5 años ☐ 10 años

Fundamentación de la necesidad de confidencialidad (obligatorio si se solicita embargo):

4.- FIRMAS

Profesor(a) guía o director(a) de memoria o tesis:

Fecha: 12-08-2026 **Firma:** ____________

Estudiante o Candidato(a):

Fecha: 12/08/2026 **Firma:** ____________

Este formulario debe ser insertado como página 2 de la memoria o tesis, completado y firmado por estudiante y profesor(a) antes de la entrega en portal PRISMA de Biblioteca USM.

Acknowledgements

La culminación de esta tesis representa el cierre de una etapa llena de desafíos, aprendizajes y experiencias que marcaron profundamente mi vida. Ningún logro de esta magnitud es el resultado del esfuerzo de una sola persona, por lo que deseo expresar mi más sincero agradecimiento a quienes me acompañaron, apoyaron y confiaron en mí a lo largo de este camino.

En primer lugar, agradezco a mi profesor guía, Dr. Esteban Gil, por brindarme la oportunidad de desarrollar esta investigación bajo su supervisión. Su confianza, orientación, disposición para compartir sus conocimientos y apoyo constante fueron fundamentales para llevar este trabajo a buen término y para mi crecimiento tanto académico como profesional.

A mi mamá, a mi papá y a toda mi familia, les debo un agradecimiento infinito. Gracias por creer siempre en mí, por apoyarme incondicionalmente en cada decisión, por alentarme a seguir adelante incluso cuando el camino parecía difícil y por enseñarme, con su ejemplo, el valor del esfuerzo y la perseverancia. Este logro es tan suyo como mío.

Quiero dedicar unas palabras muy especiales a Cristian Vera, un gran amigo que conocí durante la carrera y que lamentablemente ya no está con nosotros. Su amistad, compañerismo y calidad humana dejaron una huella imborrable en quienes tuvimos el privilegio de compartir con él. Aunque hoy no pueda acompañarnos para celebrar este momento, su recuerdo permanecerá siempre presente y forma parte de este logro.

Agradezco también a mis compañeros y amigos Cristóbal Duarte, Jorge Pettersen, Miguel Salinas, Maximiliano Trujillo, José Maripangui y Bastián Gonzales, con quienes compartí innumerables horas de estudio, trabajos, conversaciones y desafíos durante la carrera. Su apoyo, compañerismo y amistad hicieron que este recorrido fuera mucho más llevadero. Asimismo, extiendo mi gratitud a todas aquellas personas que, de una u otra forma, contribuyeron a mi formación y me tendieron una mano cuando la necesité. Cada consejo, conversación o gesto de apoyo fue importante para llegar hasta aquí.

A mi pareja, Nicole Olivares, y a mi mejor amiga, Bárbara Neira, quiero expresarles un agradecimiento muy especial. Gracias por estar presentes en los momentos más difíciles de mi vida, por brindarme contención, comprensión y ánimo cuando más lo necesitaba. Su cariño, paciencia y apoyo incondicional fueron fundamentales para superar las dificultades personales que enfrenté durante este proceso y encontrar la fortaleza necesaria para continuar.

Finalmente, agradezco el financiamiento otorgado por la Agencia Nacional de Investigación y Desarrollo (ANID) a través de los proyectos Fondecyt 1231892, CTI 250019 (SET), CIA 250006 (AC3E) y Fondequip EQM210117, cuyo apoyo hizo posible el desarrollo de esta investigación.

A todas las personas que fueron parte de este camino, ya sea desde el ámbito académico, profesional, familiar o personal, les expreso mi más profunda gratitud. Esta tesis no solo representa el resultado de años de estudio y dedicación, sino también el reflejo del apoyo, la confianza y el cariño de quienes caminaron junto a mí durante este importante capítulo de mi vida.

Resumen

Las condiciones de red débil pueden limitar la capacidad de transferencia de potencia activa de plantas eólicas basadas en generadores de inducción doblemente alimentados (DFIG), reduciendo la reserva efectivamente entregada en el punto de conexión común (PCC). Aunque la operación con reducción de potencia permite crear un margen para participar en servicios de control de frecuencia, esta reserva teórica no necesariamente coincide con la potencia adicional que puede ser transferida a la red cuando se consideran los límites de corriente de los convertidores y la fortaleza del sistema.

En este trabajo se analiza el efecto de la relación de cortocircuito (SCR) sobre la capacidad de entrega de reserva de una planta eólica DFIG. El sistema eléctrico, la planta eólica y sus controles fueron implementados en RSCAD y simulados mediante un Real-Time Digital Simulator (RTDS), considerando distintos valores de SCR, velocidades de viento, niveles de reducción de potencia (*deloading*) y regiones de operación. La operación basada en sobrevelocidad se incluyó como referencia cualitativa, mientras que la evaluación cuantitativa se concentró en los casos regulados mediante control del ángulo de paso. A partir de las simulaciones se determinaron la reserva teórica, la reserva efectiva promedio entregada durante los primeros 8 s y la razón de reserva entregada $\eta_{R,8s}$.

Los resultados muestran que la capacidad de entrega de reserva depende de la fortaleza de red y del punto de operación de la turbina. Al disminuir el SCR, aumentan las variaciones de tensión en el PCC y la corriente demandada por el convertidor del lado del rotor, reduciendo el margen disponible para la inyección de potencia activa. Cuando se alcanza el límite de corriente, parte de la potencia mecánica liberada no puede ser transferida al PCC y produce una aceleración del rotor. Para 20% de reducción de potencia y SCR igual a 1.10, $\eta_{R,8s}$ disminuyó hasta 36.10% para $V_w = 12$ m/s y hasta 46.90% para $V_w = 15$ m/s, evidenciando que el margen teórico puede sobrestimar significativamente la capacidad real de respuesta.

La razón $\eta_{R,8s}$ fue posteriormente incorporada en una evaluación económica desarrollada en Gurobi, en la que se compararon tres estrategias: *energy-only*, donde la planta participa únicamente en el mercado de energía; *naive*, donde se oferta la reserva teórica completa sin considerar su entregabilidad física; y η-*aware*, donde la oferta de reserva se limita mediante $\eta_{R,8s}$. Para $V_w = 12$ m/s, la estrategia *naive* obtuvo resultados netos mensuales incrementales respecto de *energy-only* de 99 EUR, -565 EUR y -5849 EUR al disminuir la fortaleza de la red, mientras que la estrategia η-*aware* obtuvo 1458 EUR, 1281 EUR y 388 EUR. Para $V_w = 15$ m/s, los resultados netos mensuales incrementales fueron -906 EUR, -1184 EUR y -4561 EUR para la estrategia *naive*, y 1236 EUR, 1091 EUR y 580 EUR para la estrategia η-*aware*. Estos resultados muestran que la estrategia *naive* puede generar pérdidas por incumplimiento de reserva, mientras que la estrategia η-*aware* reduce la exposición a penalizaciones y mantiene resultados positivos en todos los casos analizados.

Se concluye que la fortaleza de red y el punto de operación deben ser considerados al determinar las ofertas de reserva de plantas eólicas DFIG. El uso de la razón de reserva entregada obtenida a partir de la respuesta en el PCC permite representar de manera más realista la capacidad de respuesta de la planta y evaluar tanto la sobreestimación de la reserva como el riesgo económico asociado.

Abstract

Weak-grid conditions may limit the active-power transfer capability of wind power plants based on doubly-fed induction generators (DFIGs), reducing the reserve effectively delivered at the point of common coupling (PCC). Although deloaded operation creates an active-power margin for participation in frequency-control services, this theoretical reserve does not necessarily coincide with the additional power that can be transferred to the grid when converter-current limits and grid strength are considered.

This work analyzes the effect of the short-circuit ratio (SCR) on the reserve-delivery capability of a DFIG-based wind power plant. The power system, wind power plant, and associated control systems were implemented in RSCAD and simulated using a Real-Time Digital Simulator (RTDS), considering different SCR values, wind speeds, deloading levels, and operating regions. Overspeed-based operation was included as a qualitative reference, whereas the quantitative assessment focused on pitch-regulated operating cases. The simulations were used to determine the theoretical reserve, the average effective reserve delivered during the first 8 s, and the delivered reserve ratio $\eta_{R,8s}$.

The results show that reserve deliverability depends on both grid strength and the turbine operating point. As the SCR decreases, PCC-voltage variations and rotor-side converter (RSC) current demand increase, reducing the current margin available for active-power injection. When the converter-current limit is reached, part of the released mechanical power cannot be transferred to the PCC and instead causes rotor acceleration. For 20% deloading and an SCR of 1.10, $\eta_{R,8s}$ decreased to 36.10% for $V_w = 12$ m/s and to 46.90% for $V_w = 15$ m/s, showing that the theoretical margin may significantly overestimate the actual response capability.

The delivered reserve ratio $\eta_{R,8s}$ was subsequently incorporated into a Gurobi-based economic assessment comparing three strategies: an energy-only strategy, in which the plant participates only in the energy market; a naive strategy, which offers the full theoretical reserve without considering its physical deliverability; and an η-aware strategy, which limits the reserve bid using $\eta_{R,8s}$. For $V_w = 12$ m/s, the naive strategy yielded monthly net increments relative to the energy-only strategy of 99 EUR, -565 EUR, and -5849 EUR as grid strength decreased, whereas the η-aware strategy yielded 1458 EUR, 1281 EUR, and 388 EUR. For $V_w = 15$ m/s, the corresponding monthly net increments were -906 EUR, -1184 EUR, and -4561 EUR for the naive strategy, and 1236 EUR, 1091 EUR, and 580 EUR for the η-aware strategy. Although the absolute monthly outcomes are specific to the analyzed market period and modeling assumptions, the η-aware strategy consistently outperformed the naive strategy by reducing exposure to reserve non-delivery penalties under the evaluated weak-grid conditions.

It is concluded that grid strength and the turbine operating point should be considered when determining reserve bids from DFIG-based wind power plants. Using a PCC-level delivered reserve ratio provides a more realistic representation of the plant response capability and reduces both reserve overestimation and the associated economic risk.

Keywords: ancillary services, deloaded operation, DFIG, economic assessment, frequency control, RTDS, reserve bidding, reserve deliverability, SCR, weak-grid operation.

Table of Contents

1 Introduction

The increasing displacement of synchronous generation by converter-based renewable energy sources is reducing the equivalent inertia of modern power systems, making frequency support from these resources increasingly relevant. Wind power has received particular attention in this context because recent grid-code developments have introduced more demanding requirements for active-power control and frequency response [1–4]. Among wind generation technologies, doubly-fed induction generator (DFIG)-based wind turbines are especially relevant because their converter-based interface allows supplementary control actions for active-power regulation, frequency support, and reserve provision.

In DFIG-based wind turbines, upward frequency support can be provided through temporary kinetic-energy release or through persistent reserve created by deloaded operation. In the latter case, the turbine is intentionally operated below its maximum power point, preserving an active-power margin that can be released during under-frequency events. However, this aerodynamic headroom does not necessarily correspond to the active-power reserve that can be effectively delivered to the power system. This distinction becomes critical under weak-grid conditions, where a lower short-circuit ratio (SCR) strengthens the interaction between converter-current control, point of common coupling (PCC)-voltage dynamics, and grid impedance. As a result, converter-current limits and voltage-regulation requirements may reduce the active-current margin available for additional active-power injection [5–7].

This physical limitation also has a market implication. Ancillary-service markets remunerate reserve capacity according to the quantity offered and accepted, but actual service delivery depends on whether the committed response can actually be delivered during activation. Therefore, a wind plant that bids reserve based only on theoretical aerodynamic headroom may overestimate its deliverable capability, leading to non-delivered reserve, imbalance costs, reduced revenues, or penalty terms in a market model. Hence, reserve bidding should account for the reserve that can be transferred to the PCC under the expected grid-strength and operating conditions.

This work assesses reserve deliverability in a DFIG-based wind power plant under different SCR values, wind speeds, deloading levels, and operating regions. The main contribution is to quantify the mismatch between the reserve margin defined by deloaded operation and the reserve effectively delivered at the PCC using time-domain simulations performed in a Real-Time Digital Simulator (RTDS). The resulting delivered reserve ratio is then used as an input to an economic assessment that compares an energy-only strategy, in which no reserve is offered; a naive strategy, in which the bid is based on the full theoretical headroom; and an η-aware strategy, in which the bid is limited according to the reserve effectively deliverable at the PCC. This comparison links the physical limitations of reserve delivery with their potential economic consequences in ancillary-service markets.

Figure 1 summarizes how the physical reserve-deliverability assessment is connected to the market-oriented reserve-bidding stage. The DFIG-based wind power plant and the weak-grid power-system model are implemented in RSCAD and executed in the RTDS platform. For each operating scenario, defined by wind speed, deloading level, and SCR, the Electromagnetic Transient (EMT) simulation provides the theoretical reserve R_{th}, the effective reserve delivered at the PCC during the first 8 s after activation $R_{\text{eff},8\text{s}}$, and the delivered reserve ratio $\eta_{R,8s}$. These quantities are then used as physical inputs in the Gurobi-based optimizer to compare energy-only, naive, and η-aware Frequency Containment Reserve for Disturbances Up (FCR-D Up) bidding strategies. Therefore, the workflow should be interpreted as an offline coupling between dynamic simulation results and market assessment, rather than as a closed-loop real-time control architecture.

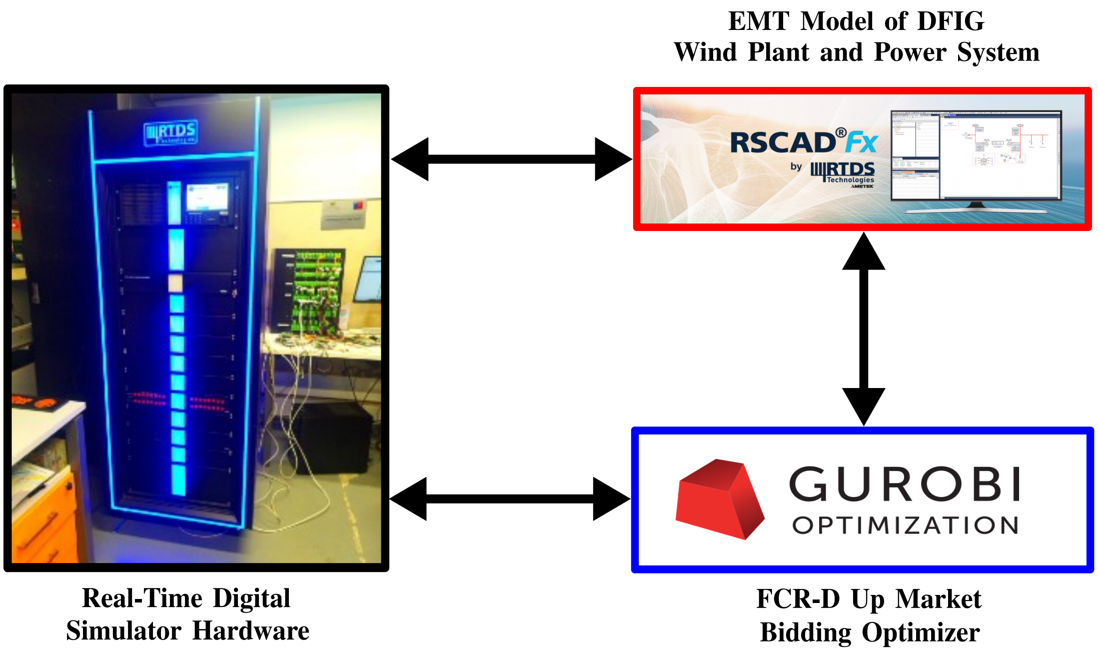

Figure 1: Offline signal-exchange workflow.

1.1 Hypothesis

A DFIG-based wind power plant can offer energy and frequency-control reserve more effectively when its operating conditions and physical limits are considered in the market assessment. Under weak-grid conditions, the reserve effectively delivered at the PCC may differ from the theoretical aerodynamic headroom; therefore, an RTDS-based delivered reserve ratio provides a more realistic estimation of the plant capability.

1.2 Research Objectives

The objectives originally presented in the TMT were refined during the development of this work. Their original scope is still fulfilled, but with a more specific focus on DFIG-based wind plants, weak-grid reserve deliverability, and FCR-D Up bidding.

1.2.1 Main Objective

Implement and evaluate, using RTDS simulations, the dynamic performance of a DFIG-based wind power plant participating in energy and frequency-control ancillary-service markets, and assess how the physical reserve effectively delivered under different operating and grid-strength conditions affects energy and reserve bidding decisions.

1.2.2 Specific Objectives

1) Implement a dynamic model of a DFIG-based wind power plant in RSCAD/RTDS, including the aerodynamic model, rotor-side converter (RSC), grid-side converter (GSC), converter-current limits, deloading operation, and frequency-control loops required for active-power reserve provision.

2) Develop an optimization-based energy and reserve bidding assessment framework for the wind power plant, incorporating market revenues, reserve penalties, and physical reserve deliverability to compare naive and η-aware strategies for FCR-D Up provision.

3) Evaluate, through RTDS simulations, the interaction between the wind plant physical model, the surrounding power system, and the frequency-control service under different operating conditions, including variations in SCR, wind speed, deloading level, and turbine operating region.

4) Quantify the mismatch between theoretical reserve and effective reserve delivered at the PCC by means of a delivered-reserve ratio obtained from the simulated active-power response after a full FCR-D Up activation request.

Table 1: Traceability between the objectives and the results subsections demonstrating their fulfillment.

Research objective	**Subsections demonstrating fulfillment**
Main objective — Assessment of reserve deliverability and its impact on bidding decisions	Subsection 5.2, "Reserve Delivery under Different SCR Levels"; Subsection 5.3, "Comparison between Theoretical and Effective Reserve"; and Subsection 5.4, "Economic Impact on Reserve-Bidding Strategies".
Specific Objective 1 — Implementation of the DFIG-based wind power plant model in RSCAD/RTDS	Subsubsection 5.2.1, "Overspeed Response in the Variable-Speed Region"; and Subsubsection 5.2.2, "Reserve Delivery in the Pitch-Regulated Region".
Specific Objective 2 — Development of the energy and reserve bidding framework	Subsubsection 5.4.2, "Bidding Outcomes".
Specific Objective 3 — Evaluation under different operating and grid-strength conditions	Subsection 5.1, "Physical Scenario Characterization"; and Subsection 5.2, "Reserve Delivery under Different SCR Levels".
Specific Objective 4 — Quantification of the mismatch between theoretical and effective reserve	Subsection 5.3, "Comparison between Theoretical and Effective Reserve".

The remainder of this thesis is organized as follows. Section 2 reviews the literature on wind-power reserve estimation, weak-grid limitations, reserve bidding, and real-time simulation, identifying the gap addressed in this work. Section 3 presents the theoretical framework, including the wind-turbine model, frequency-support strategies, and the selected reserve market. Section 4 describes the integrated methodology used to evaluate reserve deliverability through RSCAD/RTDS simulations and to incorporate the resulting physical capability into the reserve-bidding formulation. Section 5 presents and discusses the physical and economic results. Finally, Section 6 summarizes the main conclusions, limitations, and directions for future research, while the appendices provide the detailed system parameters and complementary analytical developments.

2 State of the Art

Reserve availability in wind turbines and wind farms has been addressed through different frequency-support strategies. Bubshait and Simoes quantified the reserve of a deloaded wind turbine by coordinating rotor-speed and pitch-angle control for primary frequency regulation [8]. Ouyang et al. proposed a dynamic deloading method for DFIG-based wind farms, estimating positive and negative reserve capacities according to wind speed, operating limits, forecast errors, and the reserve available from synchronous generators [9]. Du and Yu estimated future frequency-regulation potential under different operating modes using wind-speed predictions [10], while Yan et al. incorporated wind-power forecast uncertainty into the estimation of frequency-regulation capability [11]. At the wind-farm level, Tian et al. considered wake losses and optimized reserve allocation among turbines [12]. More recently, Pan et al. showed that reserve availability also depends on the adopted deloading decision, introducing decision-dependent uncertainty into the estimation problem [13]. Zhang et al. extended this concept to a frequency-constrained framework that co-optimizes energy dispatch and reserve allocation while accounting for decision-dependent uncertainties in available and reserved renewable power [14].

These studies provide relevant methods for estimating the aerodynamic and operational reserve available from wind turbines and wind farms. However, this reserve does not necessarily correspond to the additional active power that can be sustained and transferred to the grid. This distinction becomes especially relevant under weak-grid conditions. Guo et al. showed that the active-power transfer capability of a DFIG can be constrained by its power angle and rotor-current limit in very weak grids [5]. Lu et al. analyzed the dynamic P–Q capability of DFIG wind turbines considering converter-current limits, pulse-width modulation (PWM) saturation, rotor speed, and grid conditions [6], while Fedele et al. assessed how weak-grid connections and reactive-power-control strategies affect the operating capability of a DFIG [7]. These works demonstrate that grid impedance, PCC-voltage variations, reactive-power requirements, and converter limits can restrict active-power transfer. Nevertheless, they do not quantify how these constraints affect the reserve effectively delivered during a frequency-support event.

Therefore, although deloading-based reserve provision and weak-grid operation have been studied separately, the literature does not fully distinguish between the reserve margin defined at the turbine operating point and the reserve that can be dynamically transferred to the PCC. Aerodynamic and operational reserve estimates are generally formulated independently of the electrical constraints that govern the actual power transfer. Consequently, the mismatch between theoretical available reserve and effective delivered reserve under different grid-strength and operating conditions remains insufficiently addressed.

In parallel, several studies have investigated the participation of wind power in energy, reserve, and frequency-regulation markets. Soares et al. formulated offering strategies in energy and primary-reserve markets by allocating the potentially available wind generation between both products while accounting for regulation costs and penalties associated with reserve non-delivery [15]. A related formulation considered the allocation of uncertain wind generation between energy and reserve products [16]. Liang et al. proposed a combined energy and regulation-reserve market model aimed at reducing wind-power deviation penalties [17], while Edmunds et al. analyzed how market design influences wind participation in response and reserve markets [18]. Yang et al. further considered wind-power uncertainty in the participation of wind farms in energy and frequency-regulation markets [19].

More detailed reserve-bidding formulations have subsequently been proposed. Soares et al. applied stochastic programming and decision rules to manage wind uncertainty and balancing costs [20]. Hosseini et al. incorporated confidence levels associated with real-time reserve provision into day-ahead energy and reserve bidding [21], while Cao et al. used deep reinforcement learning to coordinate wind-energy bidding and reserve procurement [22]. Stratman et al. formulated an optimal strategy for participation in energy and spinning-reserve markets [23], and Hosseini et al. later proposed a multi-resolution probabilistic approach to represent fast wind variations and reserve-bid reliability [24]. Cheng et al. directly coordinated frequency-regulation control and bidding decisions for a wind-electrolysis system [25]. This study represents an important link between operational flexibility and market participation, although the wind-generation capability is described through aggregate models rather than through a detailed DFIG response under weak-grid conditions.

Recent studies have also incorporated selected physical characteristics into scheduling and market formulations. Jiang et al. jointly scheduled energy reserve and virtual inertia from wind turbines while considering rotor-speed and frequency-response requirements [26]. Jiang and Zhao incorporated wind-power inertia and reserve-control capabilities into the scheduling and pricing of frequency-regulation services [27]. Mabboux-Fort et al. included wake interactions in the joint scheduling of wind-farm energy and reserve, showing that a more realistic aerodynamic representation can modify production estimates, imbalance penalties, and market revenues [28]. These works demonstrate that physical constraints can be embedded in market models. However, they rely on reduced-order, aggregate, aerodynamic, or optimization-compatible representations and do not derive the reserve offer from the detailed electrical response of the DFIG, its converter-control loops, current limits, PCC-voltage dynamics, and grid strength.

Accordingly, the main limitation of the bidding literature is not the complete absence of physical constraints, but the limited consideration of the electrical reserve deliverability obtained from the detailed dynamic response of the wind power plant. Once aerodynamic, scheduling, uncertainty, and frequency-security constraints are satisfied, the committed reserve is generally assumed to be physically deliverable. These formulations do not explicitly evaluate the partial reserve delivery caused by the interaction between converter limits, PCC-voltage dynamics, and low-SCR grid conditions. Therefore, they do not assess how a reserve commitment based on aerodynamic headroom may perform when the active-power support effectively transferred to the PCC is lower than expected.

Real-time simulation has also been used to evaluate the physical delivery of frequency support and other ancillary services. Tuinema et al. implemented a large-scale electrolyzer model in RSCAD and assessed its frequency-support capability using RTDS [29]. Wang et al. combined FAST, digital real-time simulation, and hardware-in-the-loop (HIL) to evaluate wind-turbine inertial-control strategies while representing detailed mechanical and electrical dynamics [30]. Shao et al. employed an RTDS–GH Bladed co-simulation platform to assess inertia-emulation control in DFIG wind turbines, including inertial response, weak-grid stability, secondary frequency drops, and mechanical loading [31]. These studies provide detailed technical validation of control and frequency-support performance, but the resulting physical capability is not incorporated into a reserve-bidding or market-settlement model.

Some studies have established partial links between real-time physical simulation and economic or coordination layers. Khoshjahan and Kezunovic coupled RTDS and Typhoon-HIL models to evaluate how the delivery of a predefined spinning-reserve quantity by distributed resources affects voltages, line currents, and operating constraints in a distribution network [32]. Kezunovic et al. also proposed an HIL framework for transactive-energy exchange in a nano-grid with photovoltaic generation, battery storage, and power-electronic converters [33]. These works demonstrate that economic coordination and detailed physical simulation can be integrated. However, their applications focus on distributed resources, nanogrids, or distribution networks, and they do not close the loop between reserve bidding, detailed wind-plant dynamics, reserve delivery at the PCC, and the economic consequences of partial non-delivery.

Thus, the literature contains partial links among four elements: reserve creation through wind-turbine control, limitations on active-power transfer under weak-grid operation, economic reserve-offering strategies, and real-time assessment of ancillary-service delivery. Market-oriented studies incorporate selected physical characteristics through aggregate or reduced-order models, whereas detailed real-time studies generally stop at technical control validation. The limited works that connect physical simulation and economic coordination mainly address distributed resources and microgrid-scale applications. Within the reviewed literature, no unified framework was found that evaluates the reserve effectively delivered by a DFIG-based wind plant at the PCC under different grid-strength conditions and subsequently uses this information to assess the economic performance of its reserve-bidding strategy. This work addresses that gap by quantifying the mismatch between theoretical available reserve and effective delivered reserve using RTDS-based simulations. The resulting delivered reserve ratio is then used as an input to the economic assessment to compare a naive strategy, which assumes that the full theoretical reserve can be delivered, with an η-aware strategy, which limits the reserve bid according to the observed reserve deliverability. This approach allows the impact of physical reserve-delivery limitations on bidding outcomes, reserve shortfalls, and economic penalties to be evaluated.

3 Theoretical Framework

3.1 Wind Turbine Modeling

The mechanical power extracted from the wind is described by the aerodynamic power equation

$$P_{\text{tur}} = \frac{1}{2}\rho A V_w^3 C_p(\lambda, \beta) \tag{3.1}$$

where ρ is the air density, $A = \pi r^2$ is the swept area of the turbine blades, r is the blade radius, and V_w is the wind speed. The coefficient $C_p(\lambda, \beta)$ represents the aerodynamic efficiency of the turbine, i.e., the fraction of the available wind power converted into mechanical power.

The power coefficient depends on the pitch angle β and the tip-speed ratio λ. The latter relates the blade-tip speed to the wind speed and is defined as

$$\lambda = \frac{r\omega_{\text{tur}}}{V_w} \tag{3.2}$$

where ω_{tur} is the turbine rotor angular speed. Therefore, for a given wind speed, the extracted power is mainly determined by the rotor speed and the pitch angle through $C_p(\lambda, \beta)$.

In this work, the power coefficient is represented by the empirical expression implemented in the adopted aerodynamic model:

$$C_p(\lambda, \beta) = 0.5176\left(116\left(\frac{1}{\lambda + 0.08\beta} - \frac{0.035}{\beta^3 + 1}\right) - 0.4\beta - 5\right) e^{-21\left(\frac{1}{\lambda+0.08\beta} - \frac{0.035}{\beta^3+1}\right)} + 0.0068\lambda \tag{3.3}$$

The dimensional consistency of (3.1) is verified as follows, since $C_p(\lambda, \beta)$ is dimensionless:

$$\left[\frac{\text{kg}}{\text{m}^3}\right][\text{m}^2]\left[\frac{\text{m}^3}{\text{s}^3}\right] = \frac{\text{kg}\,\text{m}^2}{\text{s}^3} = \frac{\text{J}}{\text{s}} = \text{W} \tag{3.4}$$

Thus, (3.1) gives the mechanical power in watts. For dynamic simulations, this expression is normalized in per unit using the following rated quantities:

- GR: rated generator apparent power, in MVA.
- TR: rated turbine mechanical power, in MW.
- WSR: rated wind speed, in m/s.
- WR: ratio between rated turbine speed and rated generator speed.

The per-unit wind speed is defined as

$$V_{w,\text{pu}} = \frac{V_w}{WSR} \tag{3.5}$$

In the implemented model, the rotor speed is expressed in per unit using the rated generator speed as the base. Therefore, the turbine-side per-unit speed is obtained as

$$\omega_{\text{tur,pu}} = \frac{\omega_{\text{pu}}}{WR} \tag{3.6}$$

where ω_{pu} is the generator-side per-unit rotor speed. The parameter WR converts this speed to the turbine-side base.

Using (3.6), the tip-speed ratio can be written in per-unit form as

$$\lambda = \lambda_{\text{nom}} \frac{\omega_{\text{pu}}}{WR} \frac{1}{V_{w,\text{pu}}} \tag{3.7}$$

where λ_{nom} is the nominal tip-speed ratio. This expression gives $\lambda = \lambda_{\text{nom}}$ when $\omega_{\text{pu}} = WR$ and $V_{w,\text{pu}} = 1$.

Using the generator rated power as the system base, the turbine mechanical power in per unit is

$$P_{\text{tur,pu}} = \frac{TR}{GR} \frac{C_p(\lambda, \beta)}{C_{p,\text{max}}} V_{w,\text{pu}}^3 \tag{3.8}$$

where $C_{p,\text{max}}$ is the reference maximum power coefficient, evaluated at the nominal tip-speed ratio and zero pitch angle:

$$C_{p,\text{max}} = C_p(\lambda_{\text{nom}}, 0) \tag{3.9}$$

This formulation keeps the cubic dependence on wind speed, while $C_p(\lambda, \beta)/C_{p,\text{max}}$ represents the change in aerodynamic efficiency caused by variations in rotor speed or pitch angle.

For a fixed wind speed, the maximum power is obtained when the turbine operates at the peak of the C_p curve, that is, when $\lambda = \lambda_{\text{nom}}$ and $\beta = 0$. Under this condition, $C_p(\lambda, \beta) = C_{p,\text{max}}$, and (3.8) becomes

$$P_{\text{tur,pu}}^{\text{max}} = \frac{TR}{GR} V_{w,\text{pu}}^3 \tag{3.10}$$

From (3.7), the condition $\lambda = \lambda_{\text{nom}}$ requires

$$\omega_{\text{pu}} = V_{w,\text{pu}} WR \tag{3.11}$$

Therefore, under optimal tip-speed-ratio operation, the maximum turbine power can also be written as a cubic function of rotor speed:

$$P_{\text{tur,pu}}^{\text{max}} = \frac{TR}{GR} \frac{1}{WR^3} \omega_{\text{pu}}^3 \tag{3.12}$$

Equations (3.10) and (3.12) show that the maximum extractable power can be expressed either as a function of wind speed or, under optimal λ, as a cubic function of rotor speed.

3.2 Frequency-Control Methodologies and Reserve Provision

The frequency response strategies implemented in wind turbines can be broadly divided into temporary energy reserve methods and persistent energy reserve methods. Temporary reserve methods rely mainly on the kinetic energy stored in the rotating masses, whereas persistent reserve methods require a pre-disturbance deloaded operation to maintain an available active-power margin. Fig. 2 summarizes the main categories commonly reported in the literature.

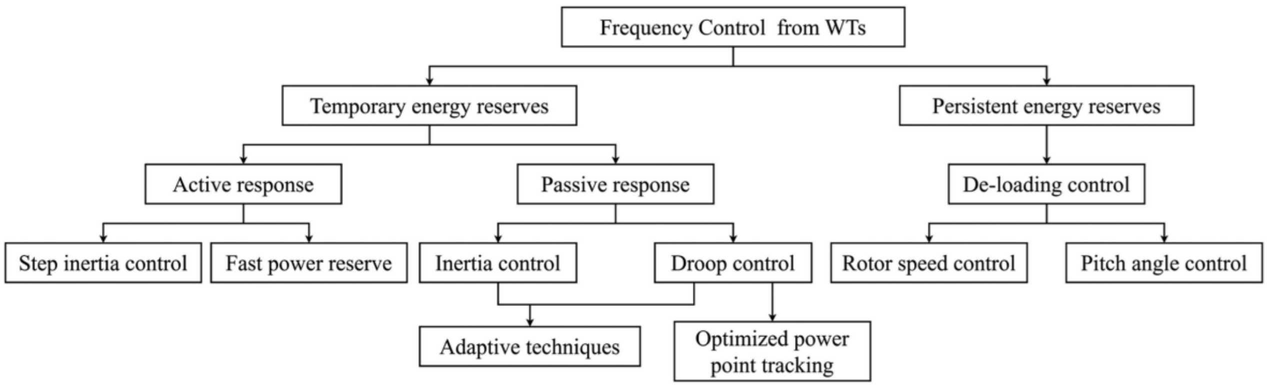

Figure 2: Categorization of frequency control from wind turbines [34].

In the case of DFIG-based wind turbines, frequency control strategies are commonly implemented through inertial response, droop-based active-power support, virtual synchronous machine emulation, and deloading control. Among these alternatives, deloading control is particularly relevant when the objective is to provide a sustained active-power reserve, since the wind turbine is intentionally operated below its maximum power point.

Since this work analyzes the active-power reserve available from a deloaded DFIG wind turbine, the following subsection focuses on the main deloading strategies: overspeed control and pitch-angle control.

3.2.1 Deloading Control

Deloading control consists of operating the wind turbine generator (WTG) below its maximum power point tracking (MPPT) condition in order to preserve an active-power margin for frequency support. In this way, the turbine does not extract all the available aerodynamic power during normal operation, allowing an additional active-power injection during under-frequency events.

The reserve margin is defined by the difference between the available power and the deloaded active-power reference. Therefore, it is important to distinguish between the reserve definition and its physical implementation. The reserve definition determines the active-power margin to be preserved, whereas the implementation determines how the turbine is moved away from the MPPT operating point, mainly through overspeed control, pitch-angle control, or a combination of both.

The active-power reserve can be expressed as

$$P_{\text{res}} = P_{\text{av}} - P_{\text{ref}}$$

where P_{res} is the preserved active-power reserve, P_{av} is the available active power, and P_{ref} is the active-power reference under deloaded operation. Commonly, P_{av} is represented by P_{MPPT}, limited by the rated power P_{Rated}.

The following methods are commonly used to define the deloaded active-power reference:

(1) Balance method [35]:
$$P_{\text{ref}} = \begin{cases} P_{\text{de}}, & P_{\text{de}} \le P_{\text{MPPT}}, \\ P_{\text{MPPT}}, & P_{\text{de}} > P_{\text{MPPT}}, \end{cases} \quad \text{with} \quad P_{\text{de}} \in [0,\ P_{\text{Rated}}]. \tag{3.13}$$

(2) Delta method [36]:
$$P_{\text{ref}} = \begin{cases} (1 - K_{\text{Reserve}})P_{\text{MPPT}}, & P_{\text{MPPT}} \le P_{\text{Rated}}, \\ (1 - K_{\text{Reserve}})P_{\text{Rated}}, & P_{\text{MPPT}} > P_{\text{Rated}}, \end{cases} \quad \text{with} \quad K_{\text{Reserve}} \in [0,\ 1]. \tag{3.14}$$

(3) Fixed reserve method [37]:
$$P_{\text{ref}} = \begin{cases} 0, & P_{\text{MPPT}} \le \Delta P_{\text{Reserve}}, \\ P_{\text{MPPT}} - \Delta P_{\text{Reserve}}, & \Delta P_{\text{Reserve}} < P_{\text{MPPT}} < P_{\text{Rated}}, \\ P_{\text{Rated}} - \Delta P_{\text{Reserve}}, & P_{\text{MPPT}} \ge P_{\text{Rated}}, \end{cases} \quad \text{with} \quad \Delta P_{\text{Reserve}} \in [0,\ \Delta P_{\text{max}}]. \tag{3.15}$$

In these expressions, P_{ref} is the active-power reference of the WTG, P_{Rated} is the rated power, P_{MPPT} is the maximum power obtained under MPPT operation, P_{de} is the imposed deloaded power command, K_{Reserve} is the reserve percentage, $\Delta P_{\text{Reserve}}$ is the fixed preserved active power, and ΔP_{max} is the maximum fixed reserve.

Fig. 3 illustrates the main mechanisms used to implement deloaded operation.

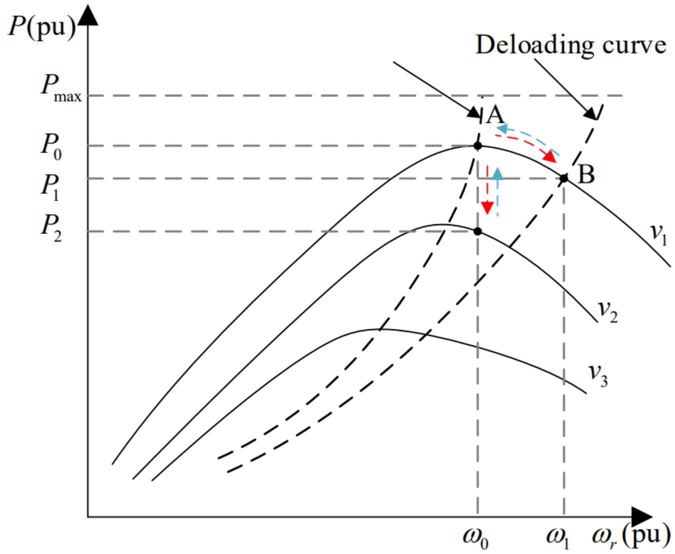

Figure 3: Deloaded operation of a wind turbine using overspeed and pitch-angle control [2].

In Fig. 3, point A represents the MPPT operating point, where the turbine extracts the maximum available power P_0. In overspeed control, the rotor speed is increased above its optimal value, moving the operating point from A to B. This reduces the active power from P_0 to P_1, preserving the difference $P_0 - P_1$ as reserve. During an under-frequency event, the rotor can be decelerated to release part of its stored kinetic energy.

In pitch-angle control, the blade pitch angle is increased to reduce the aerodynamic power coefficient and, consequently, the captured mechanical power. This also creates an active-power margin, but its response is slower because it depends on the mechanical dynamics of the pitch actuator.

Thus, overspeed control provides a fast but limited response, while pitch-angle control provides a slower but more sustained reserve, especially under medium and high wind-speed conditions. For this reason, coordinated deloading strategies often combine both mechanisms to obtain fast initial support and longer-term active-power reserve.

3.3 Electricity Markets and Reserve Bidding

Wind power plants can provide frequency-support services only if their technical capability is associated with a suitable reserve product. For a deloaded wind turbine, the selected product must be consistent with the direction and time scale of the active-power response. Since pitch-based deloading creates upward reserve by operating the turbine below its available aerodynamic power, the most suitable product is one that remunerates upward active-power response during under-frequency events.

The Finnish reserve market operated by Fingrid is used as the reference framework because it defines several frequency-control products and publishes hourly market data. Fingrid procures reserves from Balancing Service Providers to maintain the balance between generation and demand during normal operation and disturbances. The main frequency-control products are Fast Frequency Reserve (FFR), Frequency Containment Reserve for Normal Operation (FCR-N), Frequency Containment Reserve for Disturbances (FCR-D), Automatic Frequency Restoration Reserve (aFRR), and Manual Frequency Restoration Reserve (mFRR) [38]. These products differ mainly in activation speed, regulation direction, and market structure.

3.3.1 Fingrid frequency reserve products

FFR is intended for low-inertia operating conditions and requires very rapid upward response, which makes it more suitable for converter-based or storage-based resources than for pitch-only frequency support. FCR-N is used to contain small deviations around the normal frequency range and requires symmetric upward and downward regulation. FCR-D is intended for larger disturbances and is separated into FCR-D Up and FCR-D Down. FCR-D Up provides upward active-power response during under-frequency events, while FCR-D Down provides downward response during over-frequency events. Finally, aFRR and mFRR are restoration reserves used to recover the system frequency and release the faster containment reserves after the initial response.

Among these products, FCR-D Up is the most compatible with pitch-based deloading because both are associated with upward active-power support during under-frequency conditions. Table 2 summarizes the relevance of each product for the considered wind power plant.

Table 2: Fingrid frequency-control products and relevance for pitch-based deloading.

Product	Direction	Main characteristic	Relevance for pitch-based deloading
FFR	Upward	Very fast reserve for low-inertia conditions.	Not selected. Pitch actuation is too slow for this response time.
FCR-N	Upward and downward	Symmetric reserve around the normal frequency range.	Not selected. Deloading is mainly used here to create upward reserve.
FCR-D Up	Upward	Disturbance reserve for under-frequency events.	Selected. It matches the upward reserve created by pitch-based deloading.
FCR-D Down	Downward	Disturbance reserve for over-frequency events.	Not selected. It does not correspond to upward active-power support.
aFRR	Upward and downward	Automatic restoration reserve.	Possible alternative for slower control, but not the main focus.
mFRR	Upward and downward	Manual restoration reserve.	Not selected due to slower activation.

3.3.2 FCR-D Up market

FCR-D Up is an upward frequency-containment reserve used during under-frequency disturbances. Its purpose is to increase active-power injection, or equivalently reduce consumption, when the system frequency falls below the normal operating range. The activation range is associated with frequency deviations from 49.9 Hz to 49.5 Hz, where the reserve reaches full activation at the lower frequency threshold.

This product is technically aligned with pitch-based deloading. Before the disturbance, the wind turbine operates below its available aerodynamic power by increasing the pitch angle, which creates an active-power margin. During an under-frequency event, the pitch angle is reduced, aerodynamic power capture increases, and the wind plant can raise its active-power injection. Therefore, the reserve mechanism created by pitch deloading corresponds naturally to the service required by FCR-D Up.

FCR-D Up has a minimum bid size of 1 MW, and its dynamic performance is evaluated during the first seconds after activation. The Nordic technical requirements for FCR specify a short-term dynamic performance assessment for FCR-D, including the activated power after 7.5 s and the associated short-term energy response [39]. This is relevant for wind power plants because aerodynamic headroom does not necessarily guarantee that the same amount of reserve can be delivered at the PCC within the required time window.

FCR-D Up is traded as a capacity product. The provider is paid for maintaining available reserve capacity during the contracted delivery period, regardless of whether the reserve is activated. For wind power plants, this creates an opportunity cost: upward reserve can only be offered if part of the available wind power is withheld from the energy market. Therefore, the economic value of reserve provision depends on the comparison between reserve-capacity payments and the energy revenue lost due to deloaded operation.

Fingrid procures FCR-D Up through yearly and hourly markets. In the yearly market, reserve capacity is contracted in advance. In the hourly market, participants submit bids for individual delivery hours, including the offered reserve capacity in MW and the corresponding reserve price in EUR/MW. The hourly market is suitable for the economic assessment because energy and reserve-capacity prices vary from hour to hour. In this work, each wind-power operating point is evaluated separately as a fixed physical scenario over the analyzed market period.

3.3.3 FCR-D Up market data

The FCR-D Up hourly market can be represented using two public Fingrid datasets. Dataset 315 provides the hourly procured FCR-D Up volume, and dataset 318 provides the hourly FCR-D Up market price [40,41]. The procured volume characterizes the size and variability of the market and provides a reference to check whether simulated reserve bids are reasonable compared with the actual market volume. The hourly price is the main market input for the bidding model because it determines the economic value associated with the reserve capacity considered in the bidding and ex-post settlement assessment.

Table 3: FCR-D Up market data used in the bidding framework.

Element	**Role in the bidding framework**
Product	FCR-D Up, upward active-power reserve for under-frequency disturbances.
Market type	Capacity market with hourly reserve bids.
Bid information	Offered reserve capacity in MW and reserve price in EUR/MW.
Minimum bid size	1 MW for FCR-D Up.
Dataset 315	Hourly procured FCR-D Up volume. Used as a market-size reference.
Dataset 318	Hourly FCR-D Up market price. Used as the reserve-capacity price.

For a pitch-deloaded wind power plant, these market signals must be combined with the physical reserve capability of the plant. The theoretical reserve created by deloading corresponds to the aerodynamic headroom between the available power and the deloaded operating point. However, under weak-grid conditions, converter-current limits, PCC-voltage dynamics, and reduced active-power transfer capability can reduce the reserve effectively delivered to the grid. Consequently, the bidding model should rely on the reserve deliverable at the PCC, rather than on theoretical aerodynamic reserve alone.

3.3.4 Market and Modeling Assumptions

Table 4 summarizes the main assumptions used in the reserve-bidding and weak-grid assessment.

Table 4: Main assumptions used in the reserve-bidding and weak-grid assessment.

Element	**Assumption used in this work**
Market participant	Price taker; no strategic bidding or market power is modeled.
Price signals	Hourly day-ahead and FCR-D Up prices are treated as known deterministic inputs.
Wind uncertainty	Not modeled; each case uses the simulated operating point as a fixed physical input.
Market clearing	Not explicitly represented; the procured FCR-D Up volume is used only as a market-size reference.
Penalty representation	Simplified penalty term proportional to the non-delivered reserve capacity.
Grid representation	Predominantly inductive Thevenin equivalent, with $R_g \approx 0$.
Converter operation	Fixed current-priority allocation, unity-power-factor GSC operation, and fixed phase-locked loop (PLL) tuning.

The reserve-bidding model is formulated as a deterministic price-taking assessment of one DFIG-based wind power plant. The plant is assumed to have no market power and therefore takes the hourly day-ahead energy price and FCR-D Up capacity price as exogenous inputs. Consequently, the model does not represent price formation, market clearing, or competition among reserve providers. The procured FCR-D Up volume is retained only as a market-size reference and is not imposed as a binding upper bound on the reserve offer.

Perfect foresight is assumed for the economic inputs used in the monthly assessment. In particular, the hourly energy and reserve-capacity prices are treated as known deterministic signals, and wind-power uncertainty is not considered. For each scenario, the available power and the delivered reserve ratio are obtained from the corresponding RTDS/RSCAD simulation results and are then used as fixed physical inputs to the bidding problem. Therefore, the model evaluates the economic consequence of reserve-deliverability degradation under prescribed operating conditions, rather than solving a stochastic or real-time bidding problem. The adopted assumptions intentionally eliminate sources of uncertainty unrelated to reserve deliverability. As a result, differences among the evaluated strategies can be directly attributed to the physical reserve-delivery capability obtained from the RTDS simulations. Accordingly, the model should be interpreted as a scenario-based assessment of the economic implications of reserve deliverability rather than as a forecasting tool for market revenues. Incorporating uncertainty in prices, wind conditions, reserve activation, and forecasting errors constitutes a natural extension of the present framework but lies beyond the scope of this work.

The electrical network used in the weak-grid study is represented with a predominantly inductive Thevenin equivalent. The main simulations and the analytical weak-grid transfer derivation assume a practically inductive grid impedance, i.e., $R_g \approx 0$, which provides a conservative reference for active-power transfer under a given SCR. In addition, the converter control structure, current-priority allocation, unity-power-factor GSC operation, and PLL tuning are kept fixed across the analyzed cases. The conclusions should therefore be interpreted within these modeling assumptions.

4 Integrated Methodology

4.1 Physical Assessment Workflow and Reserve Metrics

Figure 4 provides an executive overview of the physical assessment stage and is placed at the beginning of the methodology because it summarizes the complete path from scenario definition to the delivered-reserve metric used later in the market model.

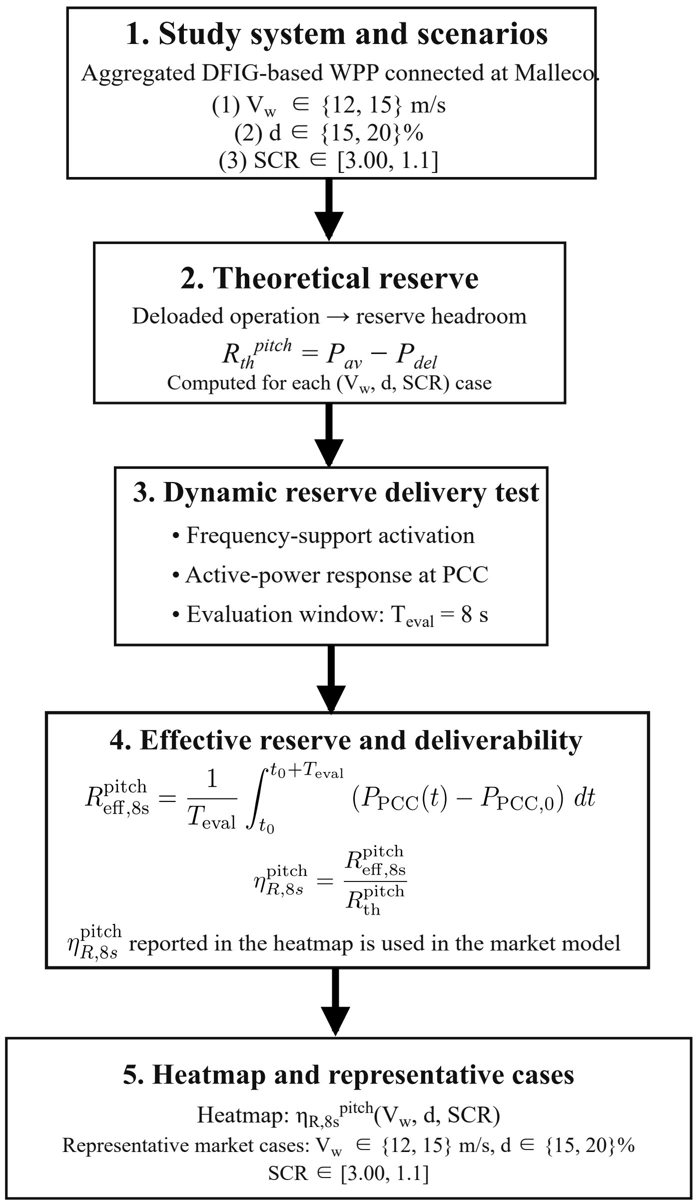

Figure 4: Executive summary of the physical reserve-deliverability assessment.

To assess reserve deliverability under weak-grid conditions, this work develops a methodology based on real-time EMT simulations using an RTDS. The analysis distinguishes between the reserve theoretically available at the wind turbine operating point and the reserve delivered at the PCC. To this end, a sensitivity analysis is carried out by varying the SCR, wind speed, deloading level, and turbine operating region.

In this work, the SCR is used as a practical indicator of grid strength at the PCC. Although grid strength cannot be fully characterized by a single static index, the SCR remains a widely used metric for classifying weak-grid conditions. In general, $SCR \geq 3$ is associated with strong-grid operation, $1 < SCR < 3$ with weak-grid operation, and $SCR \leq 1$ with very weak-grid conditions, where the stable connection of inverter-based resources may become critical [42, 43]. In this study, these thresholds are used only as reference categories for the simulated scenarios.

The wind power plant is embedded in the RSCAD multi-bus system, while the grid strength observed at the PCC is parameterized through a Thevenin-equivalent representation. The SCR is varied by modifying the associated equivalent reactance. The assumption $R_g = 0$ is adopted to represent a purely inductive grid impedance, following [5], where this condition is considered more restrictive for active-power transfer under the same SCR, and therefore conservative for evaluating reserve deliverability.

The simulations are performed using a dynamic model of a DFIG-based wind turbine developed in RSCAD. The model includes the aerodynamic conversion stage, the RSC, the GSC, and the frequency-support control loops. The current and voltage limits of both converters are explicitly represented. The detailed implementation of the model and control structures is presented in Subsection 4.3, and the parameters used to represent the DFIG system are summarized in the annex.

The simulation study is organized according to two turbine operating regions. In the overspeed region, a representative case with a wind speed of 10.0 m/s and 10% deloading is evaluated to illustrate the reserve-release mechanism in the variable-speed region. In the pitch-regulated region, wind speeds from 12 and 15 m/s are considered, with deloading levels of 15% and 20%. Each combination of wind speed, deloading level, and SCR defines a simulation scenario, allowing the influence of grid strength and turbine operating point on reserve delivery to be assessed.

For each scenario, the turbine initially operates at a pre-disturbance steady-state condition defined by the wind speed, deloading level, and SCR under consideration. In the overspeed cases, the reserve margin is created by operating the turbine below the maximum aerodynamic power point through rotor-speed adjustment. In the pitch-regulated cases, the deloaded operating point is defined by the pitch-angle reference β_0, obtained from a lookup table as a function of wind speed and deloading level.

Frequency support is activated by applying a step disturbance to the measured frequency at $t = 4$ s, reducing it from 50 Hz to 49.5 Hz. Since the frequency deviation is defined as $\Delta f = f_{ref} - f_{meas}$, this disturbance produces a positive deviation of $\Delta f = 0.01$ pu. In the implemented control scheme, this value is used as the full-reserve activation threshold, denoted as Δf_{sat}, so that the reserve request reaches its maximum value for $\Delta f \geq \Delta f_{\text{sat}}$. Therefore, the selected disturbance corresponds to a full-reserve-request condition. Smaller frequency deviations would request a proportional fraction of the available reserve, whereas larger deviations would remain saturated at the maximum reserve request. The same disturbance is applied in all cases to ensure a consistent comparison among scenarios.

During each simulation, the electrical active power delivered at the PCC, turbine mechanical power, rotor speed, PCC voltage, and converter currents are recorded. These variables are used to evaluate whether the reserve released by the control system can be transferred to the grid and dynamically sustained under low-SCR conditions.

For the pitch-regulated scenarios, the theoretical reserve, denoted as $R_{\mathrm{th}}^{\mathrm{pitch}}$, is defined as the difference between the active power available at the considered wind speed and the pre-disturbance active power associated with the deloaded operating point. This definition represents an ideal reserve margin, assuming that the available reserve can be delivered instantaneously from the pre-disturbance operating point to the post-disturbance condition. In contrast, the effective reserve, denoted as $R_{\mathrm{eff,8s}}^{\mathrm{pitch}}$, accounts for the actual transient response between these two operating points, including turbine dynamics, converter limitations, and grid interaction effects. $R_{\mathrm{eff,8s}}^{\mathrm{pitch}}$ is defined as the average increase in electrical active power delivered at the PCC during the first 8 s after frequency-support activation, with $T_{\mathrm{eval}} = 8$ s:

$$R_{\mathrm{eff,8s}}^{\mathrm{pitch}} = \frac{1}{T_{\mathrm{eval}}} \int_{t_0}^{t_0+T_{\mathrm{eval}}} \left(P_{\mathrm{PCC}}(t) - P_{\mathrm{PCC,0}}\right) dt$$

The 8 s window is selected to characterize the short-term reserve delivery following the frequency-support request, capturing the initial active-power response and the dominant pitch-actuator transient while avoiding the influence of slower recovery and rotor-speed regulation dynamics. This window is also selected as a practical simulation interval that covers the short-term response associated with the 7.5 s FCR-D dynamic-performance assessment. Based on these quantities, the delivered reserve ratio for the pitch-regulated cases is defined as

$$\eta_{R,8s}^{\mathrm{pitch}} = \frac{R_{\mathrm{eff,8s}}^{\mathrm{pitch}}}{R_{\mathrm{th}}^{\mathrm{pitch}}}$$

After obtaining the dynamic reserve-delivery results, the market assessment is performed by using R_{th}, $R_{\mathrm{eff,8s}}$, and $\eta_{R,8s}$ as physical inputs to an hourly reserve-bidding model. This stage evaluates the economic impact of reserve-deliverability degradation under weak-grid conditions. For each operating case, the theoretical reserve headroom is combined with the hourly day-ahead energy price λ_t^E and the FCR-D Up capacity price λ_t^R, considering a market resolution of $\Delta t = 1$ h. The procured FCR-D Up volume is not used as a binding optimization constraint; it is retained only as a market-size reference in the results section. Three strategies are compared: the energy-only strategy, the naive strategy based only on R_{th}, and the η-aware strategy limited by $\eta_{R,8s}$. Finally, the reserve shortfall and the corresponding penalty are evaluated ex-post to determine whether the additional FCR-D Up revenue compensates for the energy-market opportunity cost and the penalties associated with non-delivered reserve.

4.2 RSCAD/RTDS System Model

4.2.1 Complete Power-System Model and Plant Connection

Fig. 5 shows the multi-bus power-system model used as the electrical environment for the DFIG-based wind power plant. The objective of this network is not to reproduce a full market-dispatch case bus by bus, but to provide a dynamic transmission-system representation in which the wind plant is exposed to realistic interactions with synchronous generation, converter-based generation, aggregated demand, transformers, and long-distance transmission corridors.

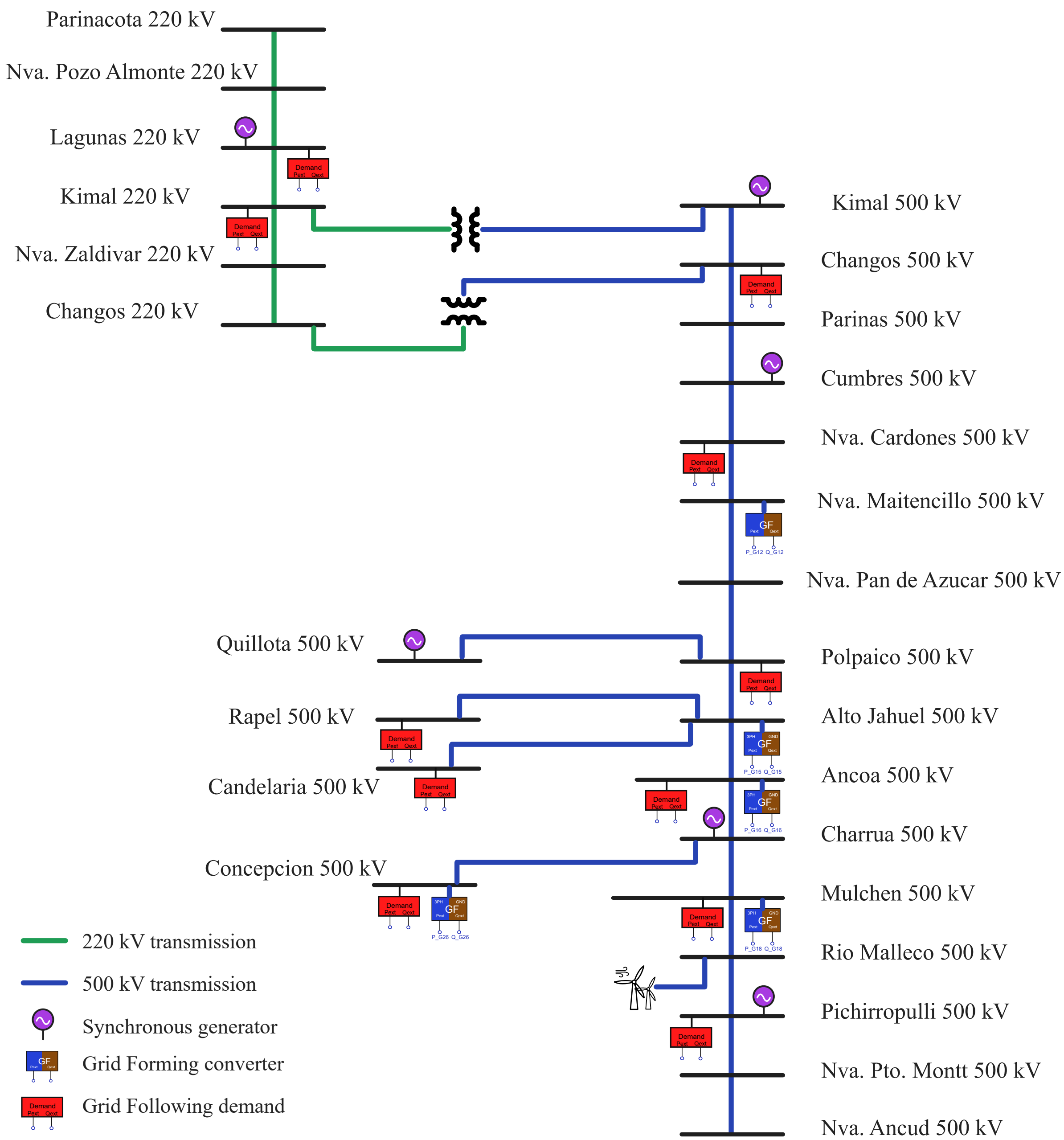

Figure 5: Complete power-system model and DFIG plant connection implemented in RSCAD.

The model includes a 220 kV subsystem and a 500 kV transmission backbone interconnected through transformer equivalents. The 220 kV side represents the northern part of the system, while the 500 kV backbone extends through the main transmission corridor where most of the dynamic interaction with the studied plant takes place. Conventional synchronous generators are included at selected buses to represent rotating inertia and voltage support. In parallel, grid-forming converter units are placed at representative 500 kV buses to emulate converter-based resources capable of imposing voltage and frequency dynamics. The remaining consumption is represented by grid-following demand blocks, which impose active and reactive-power absorption at their corresponding buses.

The DFIG-based wind power plant is connected to the 500 kV network at the bus associated with Malleco, which is used as the PCC for the reserve-deliverability assessment. From this point, the plant exchanges active and reactive power with the external network, while the converter controls use the local PCC voltage and frequency as their main electrical references. Consequently, the active-power reserve released by the turbine is not evaluated only at the machine terminals, but at the PCC, where the surrounding network strength, voltage regulation, and converter-current limits determine how much of the theoretical reserve can actually be transferred to the system. The selection of this connection point was also supported by the dynamic-performance index analysis summarized in Annex D.

This connection is important for the weak-grid analysis carried out in this work. By embedding the DFIG plant in a transmission-system model instead of connecting it to an ideal infinite bus, the simulations capture the coupling between PCC-voltage dynamics, current-priority control in the converters, and the effective active-power transfer capability. Therefore, the same frequency-support action can produce different delivered reserve ratios depending on the grid strength and operating point. This is the physical basis for using the delivered reserve ratio later in the reserve-bidding formulation.

The detailed numerical parameterization of the grid-forming units, synchronous generators, and aggregated grid-following demand was moved to Annex A. These tables are kept as traceability data for the RSCAD implementation, but they are not included in the main body because they interrupt the explanation of the model and are better suited as implementation details.

4.2.2 DFIG Converter Control Model

The overall DFIG control structure implemented in this work is shown in Fig. 6. It corresponds to a detailed RSCAD implementation of a standard vector-controlled DFIG model. The adopted PCC-voltage regulation principle is consistent with the constant-voltage control through the RSC discussed in [5]; however, the present implementation explicitly represents the inner current loops, decoupling terms, current-priority limiters, and converter voltage limits. In the RSC, stator-side electrical variables are regulated through decoupled current control in the synchronous reference frame. The i_{rd} component is associated with PCC-voltage regulation, whereas the i_{rq} component controls the electrical active power. The active-power reference is determined by the deloading strategy, the frequency deviation, and the mechanical power limits imposed by the turbine as a function of rotor speed.

On the GSC side, unity power-factor operation $(Q_{gsc} = 0)$ is assumed in order to simplify the analysis and isolate the phenomenon under study. Under this configuration, the i_{vd} component regulates the dc-link voltage, thereby regulating the active-power balance between the RSC and the GSC.

Under weak-grid conditions, the prioritization of PCC-voltage regulation and dc-link voltage stability becomes essential. Accordingly, a priority-based current allocation is enforced in both converters, giving precedence to i_{rd} in the RSC and to i_{vd} in the GSC. This strategy directly reduces the available active-current margin and, consequently, limits the deliverable active power under low-SCR operation.

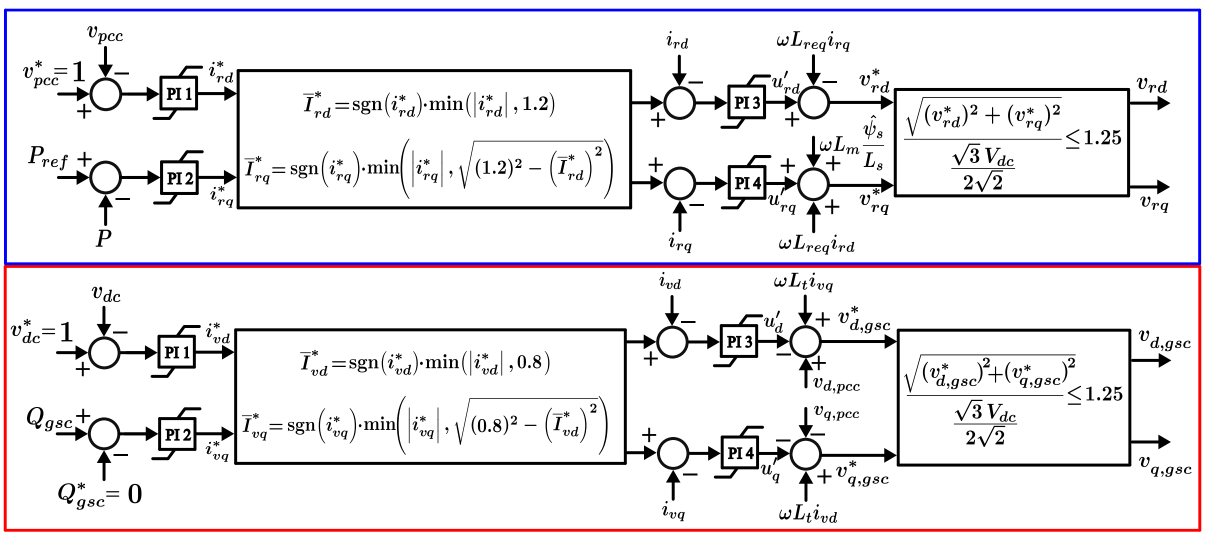

Figure 6: RSC and GSC control of the DFIG.

4.2.3 Overspeed-Based Deloading and Frequency Support

As reported in [44], frequency support in DFIG-based wind turbines can be implemented differently depending on the operating region. In the MPPT region, the available support relies on overspeed control, whereas in the pitch-regulated region, it requires coordinated pitch-angle modulation. Based on this principle, the frequency-regulation control structure implemented in this work is shown in Fig. 7. Although the overall control concept follows [44], the implementation focuses exclusively on the DFIG and incorporates a more detailed representation of the aerodynamic conversion stage. In particular, the initial pitch-angle reference β_0 is obtained from an offline lookup table, while the complete nonlinear mechanical power expression is explicitly retained to provide a more realistic representation of the reserve-activation process under weak-grid conditions.

Fig. 7 separates the control action into two branches, according to the operating region of the machine. The left branch represents the frequency-support mechanism active in the overspeed region. In this mode, the turbine is intentionally operated below the maximum aerodynamic power point, so that a reserve margin is created through deloading. In this branch, the rotor speed ω_r and the deloading factor α^{DA} define the curtailed operating point on the aerodynamic power curve and the associated reserve margin. During an under-frequency event, the frequency deviation $\Delta f = f_{ref} - f_{meas}$ is processed through the gain K_1 and the coefficient R_ω, to compute the additional power command ΔP_ω. This command is added to the pre-disturbance deloaded power P^{ener}, resulting in $P_\Sigma = P^{ener} + \Delta P_\omega$. For the overspeed-based frequency-support strategy, the rotor-speed operating range is limited to $0.8\,pu \leq \omega_r \leq \omega_{max}$, with $\omega_{max} = 1.25\,pu$. This range defines the variable-speed region in which the turbine can be intentionally deloaded with respect to the MPPT curve by operating at a higher rotor speed. As a result, an upward active-power reserve is made available for frequency-support events. Within these limits, the power-selection block determines the final active-power reference P_{ref}, ensuring that the requested power increase does not drive the turbine outside its admissible operating range.

In the overspeed region, support is provided through active-power control and kinetic energy release, whereas in the pitch-regulated region it is provided through pitch-angle reduction and increased aerodynamic power extraction. This distinction is relevant for the present study because the two operating regions involve different reserve-release mechanisms, dynamic responses, and sensitivities to weak-grid constraints.

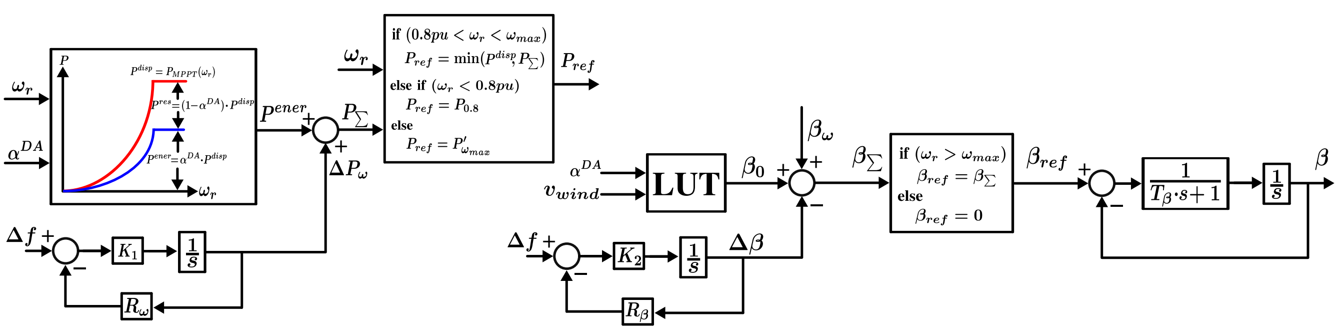

Figure 7: Primary coordinated frequency-regulation structure of the DFIG.

4.2.4 Pitch-Based Deloading and Frequency Support

The right branch of Fig. 7 represents the frequency-support mechanism active in the pitch-regulated region. This branch is enabled when the rotor speed reaches the upper operating limit, i.e., $\omega_r \geq \omega_{max} = 1.25\,pu$; for lower rotor speeds, the pitch-angle reference is kept at $\beta = 0°$. In this case, under pre-disturbance conditions, the turbine operates in a deloaded state defined by the pitch-angle reference β_0, which is obtained from a lookup table as a function of wind speed and deloading level α^{DA}. During an under-frequency event, the frequency drop produces a positive frequency deviation $\Delta f > 0$, which is processed through the gain K_2 and the coefficient R_β. In this implementation, R_β is scheduled according to the available pitch-angle margin of each pitch-regulated operating point, while K_2 defines the dynamic response of the pitch-release action. The scheduling is selected such that the full-reserve activation threshold $\Delta f_{\text{sat}} = 0.01\,pu$ produces the maximum pitch-angle reduction associated with the considered operating point. In steady state, this condition is expressed as $\Delta f_{\text{sat}}/R_\beta = \Delta\beta_{\max}$, where $\Delta\beta_{\max} = \beta_0 - \beta_{\text{ND}}$ is the available pitch-angle margin for the corresponding wind speed and deloading level. Here, β_0 is the initial deloaded pitch reference and β_{ND} is the no-deloading pitch reference obtained from the same offline aerodynamic calculation. Therefore, the frequency step from 50 Hz to 49.5 Hz commands 100% of the available reserve in the pitch-regulated cases, whereas smaller frequency deviations request a proportional fraction of it. The scheduled R_β values used in the simulated pitch-regulated cases are reported in Table 19. According to the sign convention of the summing block, the resulting signal $\Delta\beta$ acts by reducing the pitch-angle reference associated with the deloaded operating point. In the implemented scheme, the pitch-angle reference is given by $\beta_\Sigma = \beta_0 - \Delta\beta + \beta_\omega$, where β_ω is a rotor-speed correction term obtained from a proportional-integral (PI) controller acting on $\omega_r - \omega_{max}$. This term increases the pitch-angle reference when the rotor speed exceeds its upper limit, preventing excessive rotor acceleration during reserve release. Therefore, during an under-frequency event, the pitch angle is temporarily decreased with respect to β_0 when the frequency-support action dominates, increasing the aerodynamic power captured by the turbine and, consequently, the output power. The resulting signal is then applied to the pitch actuator, represented by a first-order system with time constant T_β. The pitch-rate command is constrained by a rate limiter, such that $\dot{\beta}_{\min} \leq \dot{\beta} \leq \dot{\beta}_{\max}$, and is then integrated to obtain the actual pitch angle. The final pitch angle is saturated between $\beta_{\min}$ and $\beta_{\max}$, ensuring that the pitch command remains within the physical actuator limits.

To construct the lookup table used in the reported simulations, the aerodynamic turbine model is evaluated offline for the selected pitch-regulated operating points shown in Table 5. For each selected wind speed and deloading level, the rotor speed is fixed at $\omega_r = \omega_{max} = 1.25\,pu$, and the pitch angle β is iteratively adjusted until the target deloaded mechanical power is reached. These operating points correspond to the pitch-regulated region considered in this work, where pitch-based deloading is feasible and where the electromechanical interactions affecting reserve deliverability are expected to be more significant. The calculation follows the standard aerodynamic relations of the turbine, linking wind speed, rotor speed, pitch angle, and power coefficient to obtain the corresponding deloaded operating point. The resulting β values are stored as the pre-disturbance pitch references β_0, as summarized in Table 5. The simulation scenarios analyzed in this work use the selected operating points defined in Subsection 4.4.

Table 5: Pitch-angle lookup table for the selected pitch-regulated operating points

V_w (m/s)	λ_{target}	β_{P80} (°)	β_{P85} (°)	β_{P90} (°)	β_{P95} (°)
12	8.0808	2.687	1.689	1.164	0.748
15	6.4646	13.984	13.063	12.079	11.016

Table 6 and Table 7 verify the aerodynamic operating points used to impose the 20% and 15% deloading conditions in the pitch-regulated region, respectively. In both cases, the pitch angle associated with the deloaded condition is higher than the pitch angle of the non-deloaded case. This confirms that the active-power reserve is created by intentionally reducing the aerodynamic power capture through pitch-angle displacement.

For the 20% deloading case, Table 6 shows that the ratio $C_{p,20\%}/C_{p,0\%}$ remains equal to 0.8 for the selected wind speeds. Similarly, for the 15% deloading case, Table 7 shows that $C_{p,15\%}/C_{p,0\%}$ remains equal to 0.85. Therefore, both tables validate that the offline aerodynamic calculation correctly defines the pre-disturbance deloaded operating points according to the target active-power reduction.

It is also observed that the required pitch-angle margin $\Delta\beta$ is not constant across the selected wind speeds. This occurs because the relationship between C_p, tip-speed ratio, and pitch angle is nonlinear. Consequently, the pitch variation required to achieve a given relative power reduction depends on the operating point. Comparing both deloading levels, the 20% case requires a larger pitch-angle displacement than the 15% case, as expected, since a greater reduction in aerodynamic power capture is needed. This result justifies the use of lookup tables for the initial pitch reference instead of applying a fixed pitch offset for all wind speeds.

Table 6: Pitch-angle and power-coefficient differences for 20% deloading

V_w (m/s)	λ	$\beta_{20\%}$ (°)	$\beta_{0\%}$ (°)	$\Delta\beta$ (°)	$C_{p,20\%}$	$C_{p,0\%}$	ΔC_p	$C_{p,20\%}/C_{p,0\%}$
12	8.0808	2.687	0.000	2.687	0.38401	0.48000	-0.09599	0.8000
15	6.4646	13.984	9.854	4.130	0.19661	0.24576	-0.04915	0.8000

Table 7: Pitch-angle and power-coefficient differences for 15% deloading

V_w (m/s)	λ	$\beta_{15\%}$ (°)	$\beta_{0\%}$ (°)	$\Delta\beta$ (°)	$C_{p,15\%}$	$C_{p,0\%}$	ΔC_p	$C_{p,15\%}/C_{p,0\%}$
12	8.0808	1.689	0.000	1.689	0.40801	0.48000	-0.07200	0.8500
15	6.4646	13.063	9.854	3.209	0.20890	0.24576	-0.03686	0.8500

4.3 DFIG Model Development and Control Implementation

4.3.1 Detailed DFIG Control System Implemented in RSCAD

The DFIG model is implemented in RSCAD using two back-to-back voltage-source converters: the RSC and the GSC. The converter-current notation follows Fig. 6, while the frequency-support reference structure follows Fig. 7. In the RSC, the current components are denoted as i_{rd} and i_{rq}, while in the GSC they are denoted as i_{vd} and i_{vq}. The RSC regulates the PCC voltage and the active power through i_{rd} and i_{rq}, respectively. The GSC regulates the dc-link voltage through i_{vd}, while i_{vq} is used to impose the selected reactive-power condition.

The active-power reference P_{ref} is obtained from the frequency-support block. In the overspeed region, the available power is defined as

$$P^{disp} = P_{MPPT}(\omega_r), \tag{4.16}$$

and the deloaded operating point is given by

$$P^{ener} = \alpha^{DA} P^{disp}. \tag{4.17}$$

The preserved reserve is therefore

$$P^{res} = (1 - \alpha^{DA}) P^{disp}. \tag{4.18}$$

During an under-frequency event, the frequency deviation

$$\Delta f = f_{ref} - f_{meas} \tag{4.19}$$

is processed by the overspeed support loop to generate the additional power command ΔP_ω. Following Fig. 7, this signal is added to the pre-disturbance deloaded power:

$$P_\Sigma = P^{ener} + \Delta P_\omega. \tag{4.20}$$

The final active-power reference is selected according to the rotor-speed operating range:

$$P_{ref} = \begin{cases} \min\left(P^{disp}, P_\Sigma\right), & 0.8\,pu < \omega_r < \omega_{max}, \\ P_{0.8}, & \omega_r < 0.8\,pu, \\ P'_{\omega_{max}}, & \omega_r \geq \omega_{max}. \end{cases} \tag{4.21}$$

This reference is then used by the RSC active-power loop.

For pitch-based support, the initial pitch reference β_0 is obtained from a lookup table as a function of the deloading factor α^{DA} and the wind speed v_{wind}. The frequency-support action produces a pitch reduction $\Delta\beta$, while the rotor-speed correction produces the term β_ω. Thus, the intermediate pitch command is

$$\beta_\Sigma = \beta_0 + \beta_\omega - \Delta\beta. \tag{4.22}$$

The pitch reference is then selected as

$$\beta_{ref} = \begin{cases} \beta_{\Sigma}, & \omega_r \geq \omega_{max}, \\ 0, & \omega_r < \omega_{max}. \end{cases} \tag{4.23}$$

Finally, β_{ref} is applied to the pitch actuator, represented by a first-order dynamic block with time constant T_β, followed by an integrator to obtain the actual pitch angle β.

RSC Control: The RSC control is composed of two outer loops and two inner current loops. The outer loops generate the current references i_{rd}^* and i_{rq}^*. The d-axis current component i_{rd} is used for PCC-voltage regulation, while the q-axis component i_{rq} is used for active-power regulation.

The PCC-voltage control loop is defined as

$$i_{rd}^* = G_{v,pcc}(s) \left(v_{pcc}^* - v_{pcc} \right), \tag{4.24}$$

where $v_{pcc}^* = 1\ pu$. The active-power control loop is given by

$$i_{rq}^* = G_P(s) \left(P_{ref} - P \right), \tag{4.25}$$

where P is the measured active power and P_{ref} is obtained from the frequency-support control block.

A priority-based current limiter is applied before the inner current loops. Since PCC-voltage regulation is prioritized, the d-axis rotor current is limited first:

$$\bar{I}_{rd}^* = \operatorname{sgn}\left(i_{rd}^*\right) \min\left(\left|i_{rd}^*\right|, 1.2\right). \tag{4.26}$$

The remaining current margin is assigned to the q-axis component:

$$\bar{I}_{rq}^* = \operatorname{sgn}\left(i_{rq}^*\right) \min\left(\left|i_{rq}^*\right|, \sqrt{(1.2)^2 - \left(\bar{I}_{rd}^*\right)^2}\right). \tag{4.27}$$

The inner current loops regulate i_{rd} and i_{rq}. The PI controller outputs are

$$u'_{rd} = G_{rd}(s) \left(\bar{I}_{rd}^* - i_{rd} \right), \tag{4.28}$$

$$u'_{rq} = G_{rq}(s) \left(\bar{I}_{rq}^* - i_{rq} \right), \tag{4.29}$$

where

$$G_{rd}(s) = K_{p,rd} + \frac{K_{i,rd}}{s}, \tag{4.30}$$

$$G_{rq}(s) = K_{p,rq} + \frac{K_{i,rq}}{s}. \tag{4.31}$$

The rotor-current dynamics include the cross-coupling terms associated with the synchronous reference frame. Defining the equivalent rotor inductance as

$$L_{req} = L_r - \frac{L_m^2}{L_s}, \tag{4.32}$$

the decoupled voltage references are written as

$$v_{rd}^* = u_{rd}' - \omega L_{req} i_{rq}, \tag{4.33}$$

$$v_{rq}^* = u_{rq}' + \omega L_{req} i_{rd} + \omega \frac{L_m}{L_s} \hat{\psi}_s. \tag{4.34}$$

These expressions follow the sign convention shown in Fig. 6. The terms proportional to ωL_{req} compensate the dq-axis coupling, while the term $\omega(L_m/L_s)\hat{\psi}_s$ compensates the stator-flux-induced voltage in the q-axis.

The RSC voltage reference is limited according to the converter modulation constraint:

$$\frac{\sqrt{\left(v_{rd}^*\right)^2 + \left(v_{rq}^*\right)^2}}{\frac{\sqrt{3}V_{dc}}{2\sqrt{2}}} \leq 1.25. \tag{4.35}$$

The limited voltages are denoted as v_{rd} and v_{rq}.

For completeness, the stator flux used in the feedforward term is estimated from the stator voltage equation. In the stationary $\alpha\beta$ frame,

$$\psi_{s\alpha} = \int \left(v_{s\alpha} - R_s i_{s\alpha}\right) dt, \tag{4.36}$$

$$\psi_{s\beta} = \int \left(v_{s\beta} - R_s i_{s\beta}\right) dt. \tag{4.37}$$

To avoid dc drift, a damping term is included:

$$\dot{\psi}_{s\alpha} = v_{s\alpha} - R_s i_{s\alpha} - \frac{1}{\tau_f}\psi_{s\alpha}, \tag{4.38}$$

$$\dot{\psi}_{s\beta} = v_{s\beta} - R_s i_{s\beta} - \frac{1}{\tau_f}\psi_{s\beta}. \tag{4.39}$$

The flux magnitude is then

$$\hat{\psi}_s = \sqrt{\psi_{s\alpha}^2 + \psi_{s\beta}^2}. \tag{4.40}$$

GSC Control: The GSC control follows the lower part of Fig. 6. The outer loops generate the current references i_{vd}^* and i_{vq}^*. The d-axis current i_{vd} regulates the dc-link voltage, while the q-axis current i_{vq} regulates the reactive power of the GSC. In this work, unity power-factor operation is imposed by setting

$$Q_{gsc}^* = 0. \tag{4.41}$$

The dc-link voltage control loop is

$$i_{vd}^* = G_{v,dc}(s)\left(v_{dc}^* - v_{dc}\right), \tag{4.42}$$

with $v_{dc}^* = 1\ pu$. The reactive-power control loop is

$$i_{vq}^* = G_{Q,gsc}(s)\left(Q_{gsc} - Q_{gsc}^*\right). \tag{4.43}$$

As in the RSC, a priority-based current limiter is applied. The d-axis current is limited first because dc-link voltage regulation is prioritized:

$$\bar{I}_{vd}^{*} = \operatorname{sgn}\left(i_{vd}^{*}\right)\min\left(\left|i_{vd}^{*}\right|, 0.8\right). \tag{4.44}$$

The q-axis current is then limited according to the remaining current capability:

$$\bar{I}_{vq}^{*} = \operatorname{sgn}\left(i_{vq}^{*}\right)\min\left(\left|i_{vq}^{*}\right|, \sqrt{(0.8)^2 - \left(\bar{I}_{vd}^{*}\right)^2}\right). \tag{4.45}$$

The GSC is connected to the PCC through an RL filter with resistance R_t and inductance L_t. Using the notation of Fig. 6, the inner current controller outputs are

$$u_d' = G_{vd}(s)\left(\bar{I}_{vd}^{*} - i_{vd}\right), \tag{4.46}$$
$$u_q' = G_{vq}(s)\left(\bar{I}_{vq}^{*} - i_{vq}\right), \tag{4.47}$$

where

$$G_{vd}(s) = K_{p,vd} + \frac{K_{i,vd}}{s}, \tag{4.48}$$
$$G_{vq}(s) = K_{p,vq} + \frac{K_{i,vq}}{s}. \tag{4.49}$$

The voltage references generated by the inner current loops are

$$v_{d,gsc}^{*} = -u_d' + \omega L_t i_{vq} + v_{d,pcc}, \tag{4.50}$$
$$v_{q,gsc}^{*} = -u_q' - v_{q,pcc} + \omega L_t i_{vd}. \tag{4.51}$$

These expressions keep the same sign convention used in Fig. 6. The voltage feedforward terms are $v_{d,pcc}$ and $v_{q,pcc}$, while the terms proportional to ωL_t compensate the cross-coupling of the filter dynamics.

The GSC voltage reference is limited according to

$$\frac{\sqrt{\left(v_{d,gsc}^{*}\right)^2 + \left(v_{q,gsc}^{*}\right)^2}}{\frac{\sqrt{3}V_{dc}}{2\sqrt{2}}} \leq 1.25. \tag{4.52}$$

The limited converter voltages are denoted as $v_{d,gsc}$ and $v_{q,gsc}$.

The active and reactive powers of the GSC are computed in the synchronous reference frame as

$$P_{gsc} = v_{d,pcc} i_{vd} + v_{q,pcc} i_{vq}, \tag{4.53}$$
$$Q_{gsc} = v_{q,pcc} i_{vd} - v_{d,pcc} i_{vq}. \tag{4.54}$$

When the PLL aligns the d-axis with the PCC voltage vector, $v_{q,pcc} = 0$, and therefore

$$P_{gsc} = v_{d,pcc} i_{vd}, \tag{4.55}$$
$$Q_{gsc} = -v_{d,pcc} i_{vq}. \tag{4.56}$$

Under this convention, increasing i_{vq} reduces Q_{gsc}. This is why the reactive-power controller is written using the error $Q_{gsc} - Q_{gsc}^{*}$, as shown in Fig. 6.

4.4 Selected Scenarios

The selected scenarios are defined to evaluate reserve deliverability under different turbine operating regions, deloading levels, and grid-strength conditions. Two operating regions are considered: the overspeed region and the pitch-regulated region. In the overspeed region, a case with a wind speed of $10.0\,\mathrm{m/s}$ and 10% deloading is evaluated, whereas in the pitch-regulated region, wind speeds of $12\,\mathrm{m/s}$ and $15\,\mathrm{m/s}$ are considered. For the pitch-regulated region, deloading levels of 15% and 20% are analyzed.

The deloading levels considered in this work, 10% for the overspeed region and 15% and 20% for the pitch-regulated region, are consistent with the range of power margins reported in the literature for wind power frequency regulation [45]. Each operating point is evaluated under multiple SCR values in order to assess the effect of grid strength on reserve delivery. The selected scenarios enable a systematic comparison of reserve deliverability across different wind speeds, deloading levels, turbine operating regions, and grid-strength conditions. This makes it possible to identify how the effective reserve delivered at the PCC varies not only with SCR, but also with the turbine operating region and the selected deloading level.

It should be noted that the overspeed-based and pitch-regulated cases involve different reserve-release mechanisms and different pre-disturbance operating conditions. Therefore, the comparison presented in this work is not intended to provide a direct ranking of deloading control strategies, but rather to illustrate how weak-grid conditions affect reserve deliverability within each operating region.

4.5 Reserve Bidding Formulation

The reserve-bidding formulation translates the reserve-deliverability assessment into an hourly market decision problem. The objective is to determine how much active power should be scheduled in the energy market and how much FCR-D Up reserve should be offered, while accounting for the fact that the theoretical aerodynamic reserve may not be fully deliverable at the PCC.

Figure 8 summarizes the economic stage of the methodology. This overview is located in the reserve-bidding subsection because it links the delivered reserve ratio obtained from the physical assessment, $\eta_{R,8s}$, with the ex-ante bidding decision and the ex-post penalty assessment.

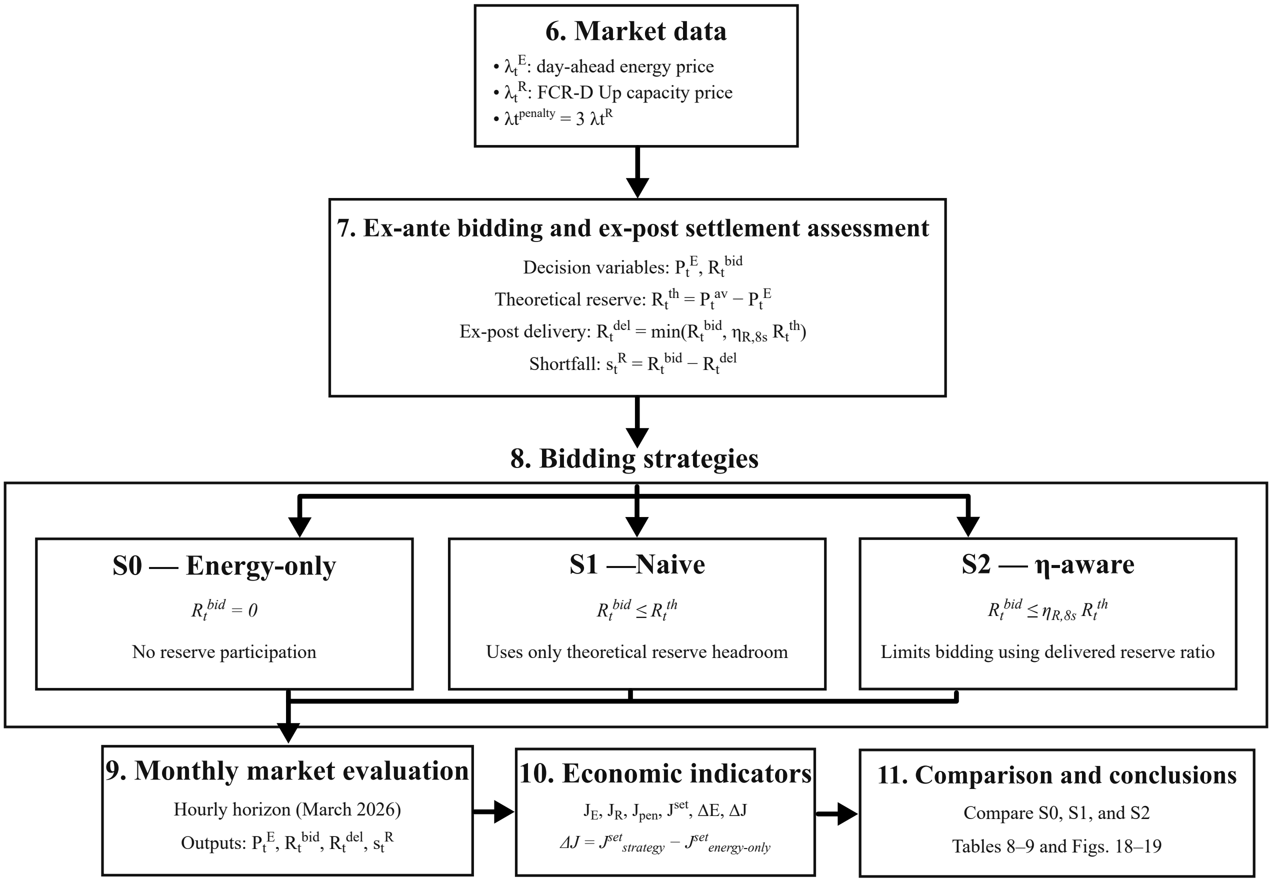

Figure 8: Executive summary of the reserve-bidding and economic assessment (continued from Fig. 4).

The bidding horizon is represented by the set of delivery hours $\mathcal{T}$. For each hour $t \in \mathcal{T}$, the wind power plant decides the scheduled active power P_t^E and the reserve capacity offered to the FCR-D Up market R_t^{bid}. The hourly energy price is denoted by λ_t^E, while the FCR-D Up capacity price is denoted by λ_t^R. The day-ahead energy price λ_t^E is obtained from the ENTSO-E Transparency Platform energy-prices dataset for the Finnish bidding zone [46], while λ_t^R is obtained from Fingrid dataset 318 [41]. The procured FCR-D Up volume from Fingrid dataset 315 is used as a reference for the market size [40].

For a given available wind power P_t^{av}, the theoretical reserve created by deloaded operation is defined as

$$R_t^{\text{th}} = P_t^{\text{av}} - P_t^E. \tag{4.57}$$

This reserve corresponds to the aerodynamic headroom between the available power and the scheduled active power. However, the simulations show that only a fraction of this headroom may be effectively delivered at the PCC under weak-grid conditions. Therefore, the reserve actually delivered during the response window is evaluated as

$$R_t^{\text{del}} = \min\left(R_t^{\text{bid}}, \eta_{R,8s} R_t^{\text{th}}\right), \tag{4.58}$$

where $\eta_{R,8s}$ is the delivered reserve ratio obtained from the dynamic simulations.

To explicitly represent the economic consequence of overestimating the reserve capability, a reserve shortfall variable s_t^R is introduced as

$$s_t^R = R_t^{\text{bid}} - R_t^{\text{del}}, \tag{4.59}$$

where $s_t^R \geq 0$ represents the reserve capacity that was offered but not effectively delivered. Following the Fingrid FCR terms and conditions, the penalty associated with non-delivered reserve capacity is represented as three times the FCR capacity price multiplied by the undelivered capacity [47]. This term is used as a simplified penalty representation for the reserve-bidding assessment rather than as a complete market-settlement model. Thus, the hourly penalty is defined as

$$S_t^{\text{FCR}} = 3\lambda_t^R s_t^R \Delta t, \tag{4.60}$$

where λ_t^R is the FCR-D Up capacity price, s_t^R is the non-delivered reserve capacity, and Δt is the market time step. After the ex-ante reserve bid is obtained, the delivered reserve, the non-delivered reserve, and the corresponding penalty are evaluated ex-post. Therefore, the following expression is used as the settlement metric for comparing the different bidding strategies:

$$J^{\text{set}} = \sum_{t \in \mathcal{T}} \left(\lambda_t^E P_t^E + \lambda_t^R R_t^{\text{del}} - 3\lambda_t^R s_t^R \right) \Delta t. \tag{4.61}$$

where $\Delta t = 1$ h for the hourly FCR-D Up market. This settlement metric is used only after the bid has been placed, in order to quantify the economic effect of reserve non-delivery. The ex-ante bidding decision is represented separately through the energy revenue and the reserve-capacity value associated with the offered reserve:

$$J^{\text{bid}} = \sum_{t \in \mathcal{T}} \left(\lambda_t^E P_t^E + \lambda_t^R R_t^{\text{bid}} \right) \Delta t. \tag{4.62}$$

The distinction is important because the naive strategy does not use the delivered-reserve constraint when placing the bid. Therefore, R_t^{del}, s_t^R, and the penalty term are computed only in the ex-post assessment. In contrast, the η-aware strategy includes the derating factor $\eta_{R,8s}$ directly in the bid constraint. The ex-ante bidding and ex-post settlement assessment are described by the following relations:

$$0 \leq P_t^E \leq P_t^{\text{av}}, \quad \forall t \in \mathcal{T}, \tag{4.63}$$

$$R_t^{\text{th}} = P_t^{\text{av}} - P_t^E, \quad \forall t \in \mathcal{T}, \tag{4.64}$$

$$0 \leq R_t^{\text{bid}} \leq R_t^{\text{th}}, \quad \forall t \in \mathcal{T}, \tag{4.65}$$

$$R_t^{\text{bid}} = R_t^{\text{del}} + s_t^R, \quad \forall t \in \mathcal{T}, \tag{4.66}$$

$$s_t^R \geq 0, \quad \forall t \in \mathcal{T}. \tag{4.67}$$

Constraint (4.65) allows the plant to submit reserve bids based on the theoretical aerodynamic headroom. The delivered reserve is then evaluated ex-post using (4.58), according to the simulated delivered reserve ratio. If the bid exceeds the deliverable reserve, the deficit appears through s_t^R and reduces the ex-post settlement value through the penalty term in (4.61).

The FCR-D Up minimum bid size can be included by introducing a binary participation variable z_t. In that case, the bid must satisfy

$$R^{\min} z_t \leq R_t^{\text{bid}} \leq \overline{R}_t z_t, \quad \forall t \in \mathcal{T}, \tag{4.68}$$

$$z_t \in \{0, 1\}, \quad \forall t \in \mathcal{T}, \tag{4.69}$$

where $R^{\min} = 1$ MW for FCR-D Up. In the main formulation, the upper bound $\overline{R}_t$ is determined by the physical reserve capability of the wind power plant, not by an assumed share of the total procured market volume. Thus, for a naive bid the relevant upper bound is the theoretical reserve R_t^{th}, whereas for an η-aware bid it is the effective reserve capability $\eta_{R,8s} R_t^{\text{th}}$. The hourly procured FCR-D Up volume is therefore not included as a binding constraint in the optimization model. It is used only as a market-size reference in the results section, because this work does not model strategic bidding, market clearing, or competition among reserve providers.

The formulation allows three bidding strategies to be compared. The first is the energy-only strategy, in which the wind power plant participates only in the day-ahead energy market and no reserve is offered:

$$R_t^{\text{bid}} = 0 \tag{4.70}$$

The second is the naive strategy, in which the ex-ante reserve bid is allowed to use the full theoretical reserve R_t^{th} without considering the physical deliverability constraint. In this case, the plant may obtain higher reserve-capacity revenue, but any non-delivered reserve is penalized in the ex-post settlement through the Fingrid-based penalty term associated with s_t^R. The third is the η-aware strategy, in which the reserve bid is directly limited by the delivered reserve ratio:

$$R_t^{\text{bid}} \leq \eta_{R,8s} R_t^{\text{th}} \tag{4.71}$$

The comparison between these strategies quantifies the economic impact of weak-grid reserve degradation. A naive bid may overestimate the plant capability and lead to reserve shortfalls when $\eta_{R,8s} < 1$. In contrast, the η-aware bid reduces the offered FCR-D Up capacity according to the reserve that can actually be delivered at the PCC, avoiding or reducing the penalty associated with non-delivered reserve. Therefore, the bidding model links the physical reserve-delivery limitation observed in the simulations with its economic consequence in the reserve market.

5 Results

5.1 Physical Scenario Characterization

The physical results are organized from the operating-point definition to the economic consequence of reserve-delivery degradation. Table 8 summarizes the cases used to identify the reserve-release mechanisms before comparing the theoretical and effective reserve.

Table 8: Characterization of the physical scenarios used in the reserve-deliverability assessment.

Operating region	Wind speed	Deloading	Purpose in the results
Variable-speed/overspeed	10.0 m/s	10%	Reference case for kinetic-energy-supported reserve release and identification of the minimum SCR at which the adopted PLL remains synchronized.
Pitch-regulated	12 m/s	15% and 20%	Evaluation of the interaction among pitch release, converter-current limits, PCC-voltage dynamics, and reserve delivery.
Pitch-regulated	15 m/s	15% and 20%	Assessment of operating-point sensitivity near rated-power operation and input to the economic comparison.

5.2 Reserve Delivery under Different SCR Levels

5.2.1 Overspeed Response in the Variable-Speed Region

This case serves as a reference for the variable-speed region, providing context for the pitch-regulated results analyzed in the following subsections. The overspeed operating condition at 10.0 m/s with 10% deloading is used as a representative scenario. Fig. 9 shows the electrical and mechanical power responses during reserve delivery under SCR = 1.20. In this case, the electrical power increases after reserve activation and tracks the mechanical power closely, confirming that the reserve can be effectively delivered. A temporary mismatch between P_e and P_{mec} is observed during the transient, indicating that part of the power response is supported by the release of stored rotational kinetic energy. For SCR values above 0.90, the overspeed-based reserve delivery remained largely unaffected, with no significant reduction in delivered active power observed as grid strength changed. Below this threshold, the PLL was unable to properly track the grid phase reference.

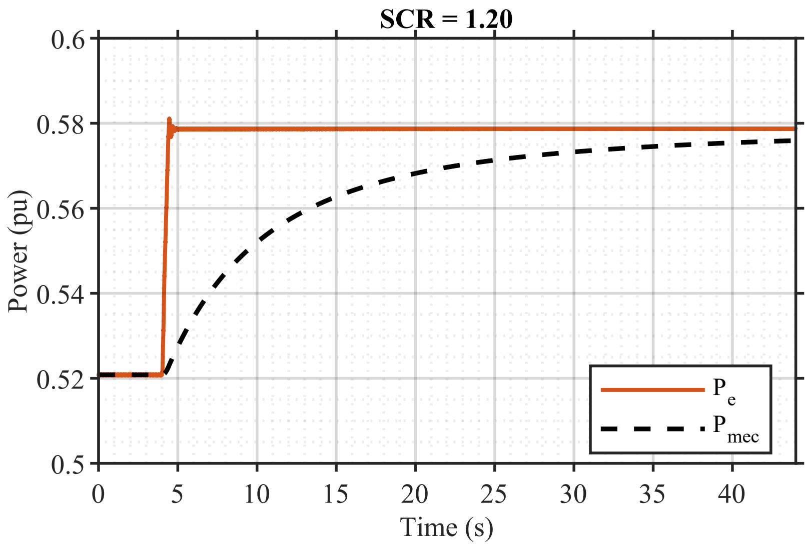

Figure 9: Mechanical and electrical power responses for the $10.0\ \mathrm{m/s}$ case with 10% deloading under SCR = 1.20.

This behavior contrasts with the pitch-regulated cases, where reserve deliverability degrades progressively with decreasing SCR through a different set of mechanisms. This distinction is analyzed in detail in the following subsections.

5.2.2 Reserve Delivery in the Pitch-Regulated Region

This subsection analyzes a representative pitch-regulated operating point to identify the dynamic mechanisms responsible for reserve-delivery degradation under weak-grid conditions. The selected case corresponds to a wind speed of 12 m/s and 20% deloading, for which the dynamic waveforms are shown at SCR = 3.00, SCR = 1.70, and SCR = 1.20. These values are selected to illustrate the transition from strong-grid operation to weaker-grid conditions and to reveal how converter limits, PCC-voltage dynamics, and electromechanical imbalance interact as the grid strength decreases. The delivered-reserve ratios used in the economic assessment are taken from the heatmap in Fig. 14; therefore, the market tables use the SCR points available in that heatmap for the selected economic cases.

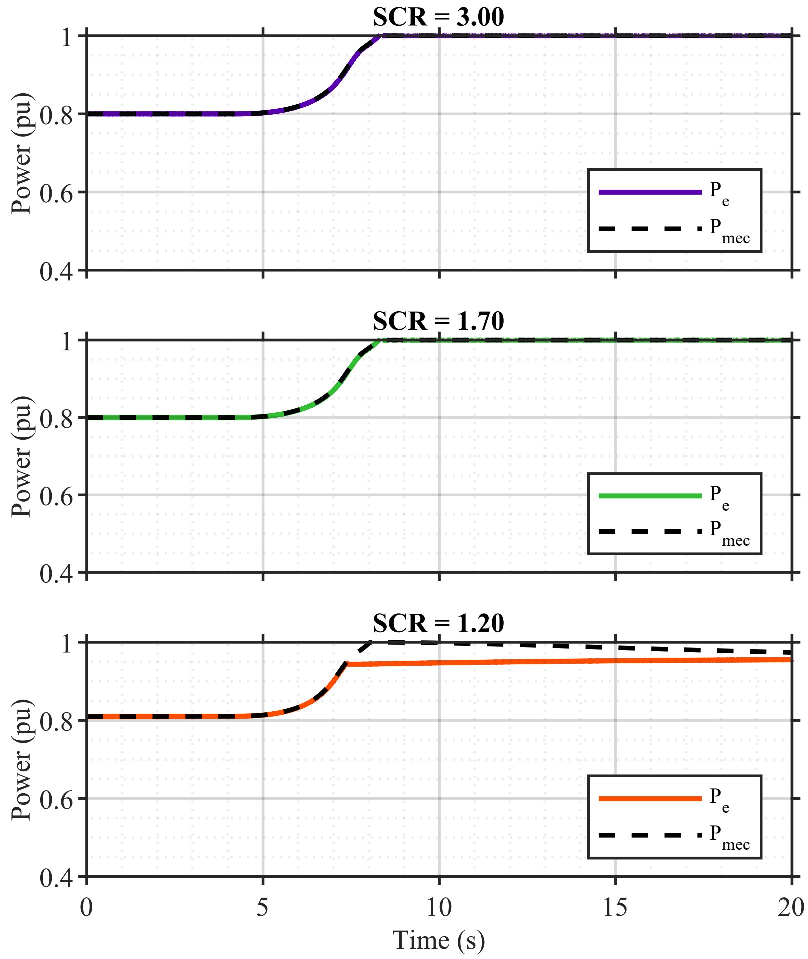

Figure 10: Electrical and mechanical power responses for the 12 m/s, 20% deloading case under different SCR values.

Fig. 10 compares the electrical power P_e and the mechanical power P_{mec} for each SCR value. This comparison is particularly relevant because it directly illustrates the power imbalance that emerges as the network becomes weaker. For SCR = 3.00, both signals remain closely aligned during the post-disturbance interval, indicating that the released reserve is effectively transferred to the grid. For SCR = 1.70, the response remains close to the strong-grid case, although small differences are observed. For SCR = 1.20, the electrical power remains below the mechanical power during a significant part of the response, indicating that the released mechanical power cannot be fully transferred to the grid under this weak-grid condition.

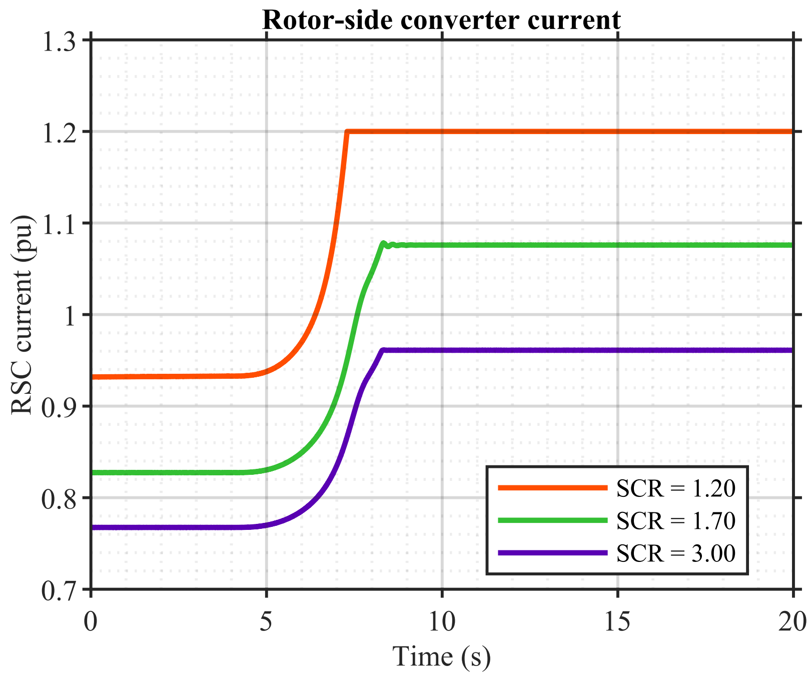

Figure 11: RSC current for the 12 m/s, 20% deloading case under different SCR values.

Fig. 11 presents the RSC current. As the SCR decreases, the current required by the RSC increases. For SCR = 1.20, the current reaches the imposed rotor-current limit, indicating that converter-current saturation becomes a key constraint on the sustained transfer of active power to the grid. This is consistent with the reduced delivered reserve ratio observed in the low-SCR cases.

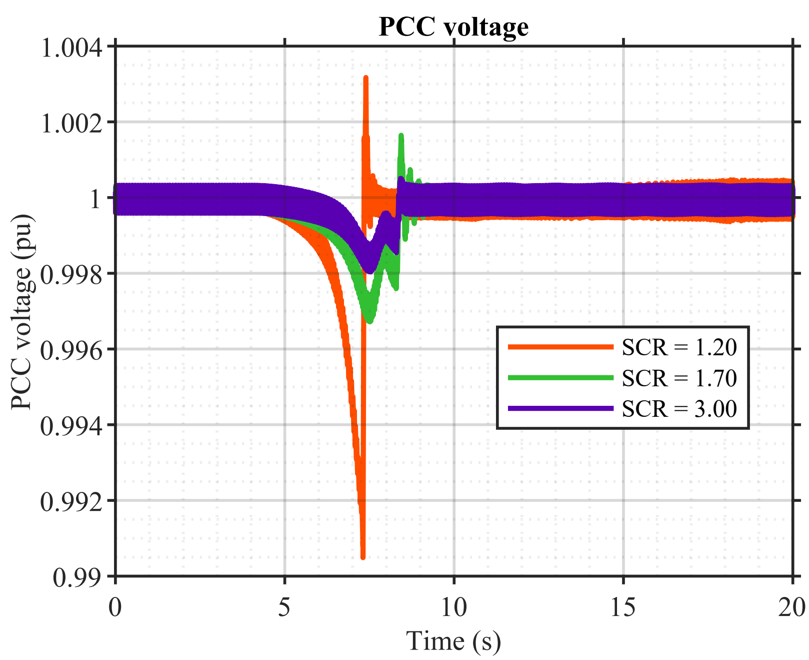

Figure 12: PCC voltage response for the 12 m/s, 20% deloading case under different SCR values.

Fig. 12 shows the PCC voltage response. It can be seen that under strong-grid conditions, the voltage remains close to its nominal value. As the SCR decreases, the voltage disturbance becomes more pronounced, with the largest voltage excursion observed for SCR = 1.20. This indicates that the active-power response is accompanied by stronger PCC-voltage dynamics as the grid becomes weaker.

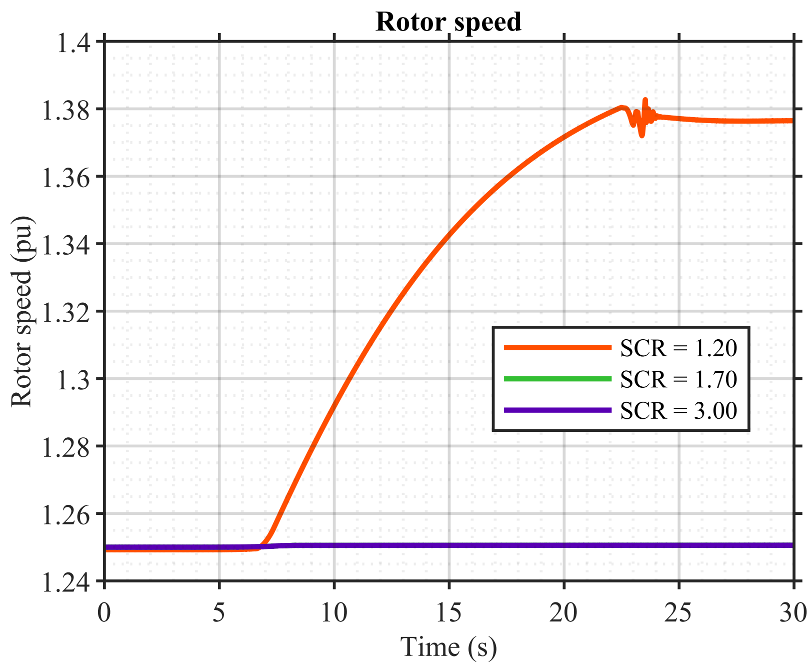

Figure 13: Rotor-speed response for the 12 m/s, 20% deloading case under different SCR values.

Finally, Fig. 13 presents the rotor-speed evolution. The lowest-SCR case exhibits the largest speed increase, which is consistent with the power imbalance observed in Fig. 10. Since P_{mec} remains temporarily above P_e during a significant part of the response, the resulting imbalance accelerates the rotor instead of being fully delivered to the grid. Therefore, the rotor-speed rise should be interpreted primarily as a consequence of the limited electrical power transfer capability under weak-grid conditions, rather than as the main cause of reserve-delivery degradation.

Taken together, Figs. 10–13 indicate that the reduction of reserve delivery at low SCR is associated with a coupled mechanism: weak-grid conditions lead to stronger PCC-voltage dynamics, increased RSC current demand, operation close to the current limit, a reduced capability to sustain electrical active-power transfer to the grid, and a consequent increase in rotor kinetic energy. This also clarifies why the delivered reserve ratio reported in Fig. 14 should be interpreted as a short-term reserve-delivery metric over the first 8 s after activation: this interval is intended to quantify the initial reserve-release capability. Consequently, the delivered reserve ratio is not intended to represent the final steady-state reserve capability. Instead, it quantifies the average active-power support effectively delivered at the PCC during the initial 8 s following the full-reserve request, when the interaction between pitch release, converter-current limits, PCC-voltage dynamics, active-power transfer, and rotor acceleration is most relevant.

It should be noted that the results are specific to the adopted control structure, grid configuration, and impedance assumptions; alternative reactive-power control strategies, current-priority schemes, or nonzero grid resistance may modify the relative importance of the identified constraints and the degree of reserve degradation.

5.3 Comparison between Theoretical and Effective Reserve

This subsection compares the delivered reserve ratio obtained in the pitch-regulated operating region. Fig. 14 provides a global view of $\eta_{R,8s}$ across the selected wind speeds, deloading levels, and SCR values. Table 9 reports the representative operating cases used in the market assessment. The numerical values are consistent with the heatmap, which is the reference source for $\eta_{R,8s}$ throughout the economic analysis.

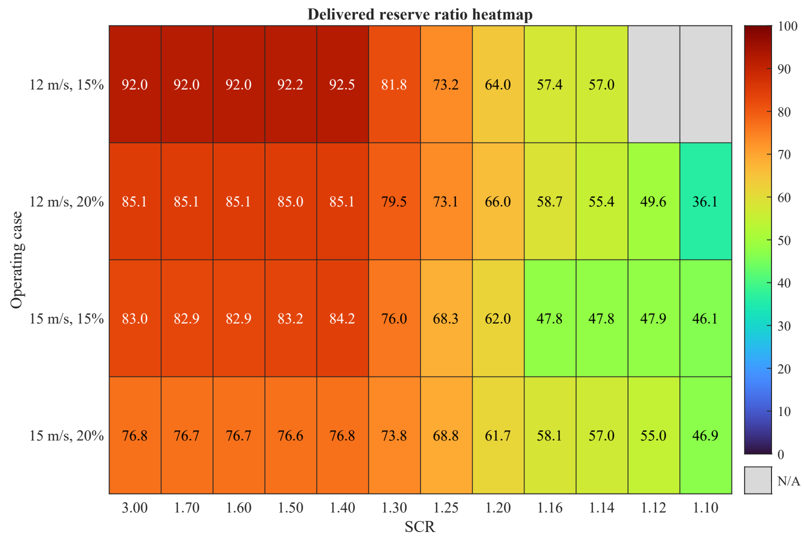

Figure 14: Heatmap of the delivered reserve ratio $\eta_{R,8s}$ (%) across the selected pitch-regulated operating cases and SCR values. Gray cells indicate cases that became unstable due to the weak-grid condition.

Table 9: Theoretical and effective reserve deployed for representative operating cases

Case	SCR	R_{th} (pu)	$R_{\text{eff},8s}$ (pu)	$\eta_{R,8s}$ (%)
12 m/s, 15%	3.00	0.150	0.138	92.05
12 m/s, 15%	1.30	0.140	0.115	81.79
12 m/s, 15%	1.14	0.148	0.084	56.99
12 m/s, 20%	3.00	0.200	0.170	85.13
12 m/s, 20%	1.30	0.196	0.156	79.50
12 m/s, 20%	1.10	0.202	0.073	36.10
15 m/s, 15%	3.00	0.150	0.125	82.98
15 m/s, 15%	1.30	0.149	0.114	75.96
15 m/s, 15%	1.25	0.153	0.105	68.30
15 m/s, 20%	3.00	0.200	0.154	76.76
15 m/s, 20%	1.30	0.188	0.139	73.82
15 m/s, 20%	1.10	0.203	0.095	46.90

Fig. 14 reveals a clear dependence of reserve deliverability on both the turbine operating point and grid strength. The pitch-regulated cases exhibit a heterogeneous and operating-point-dependent behavior. For high SCR values, several operating points show relatively high delivered reserve ratios. For instance, the 12 m/s case with 15% deloading reaches $\eta_{R,8s} = 92.05\%$ at SCR = 3.00, while the 12 m/s case with 20% deloading reaches $\eta_{R,8s} = 85.13\%$ under the same grid condition, as reported in Table 9. However, this performance is not preserved across all pitch-regulated operating points as the grid weakens.

For the 15 m/s case with 20% deloading, the delivered reserve ratio decreases from 76.76% at SCR = 3.00 to 46.90% at SCR = 1.10. Overall, these results demonstrate that the theoretical reserve can substantially overestimate the reserve that is effectively delivered at the PCC under weak-grid conditions, and that this mismatch is governed by the combined effect of wind speed, deloading level, and SCR rather than by any single factor alone.

5.4 Economic Impact on Reserve-Bidding Strategies

5.4.1 Market Inputs

This section summarizes the market signals used to contextualize the reserve-bidding formulation. The economic assessment should be interpreted as a scenario-based comparison intended to isolate the effect of reserve deliverability rather than as a prediction of commercial performance. The available data include the hourly procured FCR-D Up volume, the corresponding FCR-D Up capacity price, and the day-ahead energy price for the same analysis period. The capacity price and the day-ahead energy price are the economic inputs used in the reserve-bidding assessment, while the procured FCR-D Up volume is retained only as a market-size reference. Therefore, the volume signal is not imposed as a binding constraint in the optimization problem; it is shown to indicate the scale and variability of the hourly FCR-D Up market.

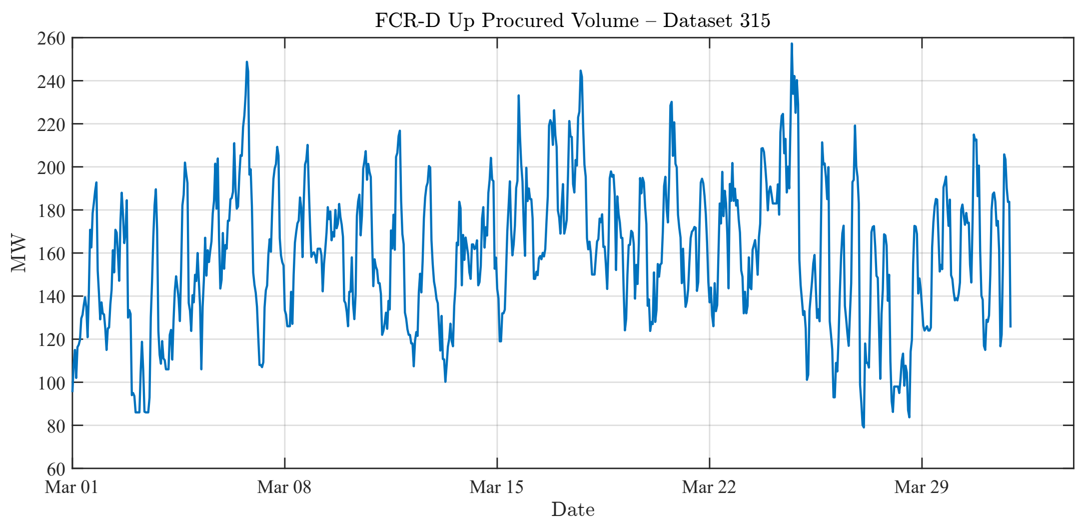

Figure 15: Hourly procured FCR-D Up volume from Fingrid dataset 315 for March 2026. This signal is used only as a market-size reference and is not included as a binding constraint in the optimization model.

Fig. 15 is kept to provide a scale reference for the hourly FCR-D Up market. It is not used to limit the reserve bid through a fixed market-share parameter. In other words, no constraint of the form $R_t^{\text{bid}} \leq$

$\gamma V_t^{\mathrm{FCRD}}$ is imposed in the main optimization model. The reserve offer is instead bounded by the plant's theoretical headroom or by its effective reserve capability, depending on the bidding strategy considered.

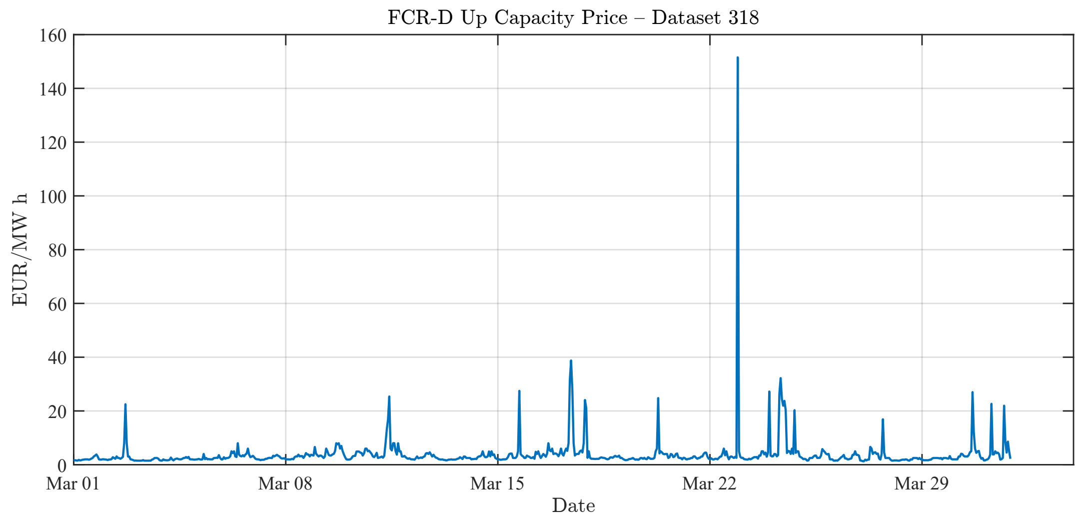

Figure 16: Hourly FCR-D Up capacity price from Fingrid dataset 318 for March 2026. This price is used as the reserve-capacity revenue term λ_t^R in the bidding formulation.

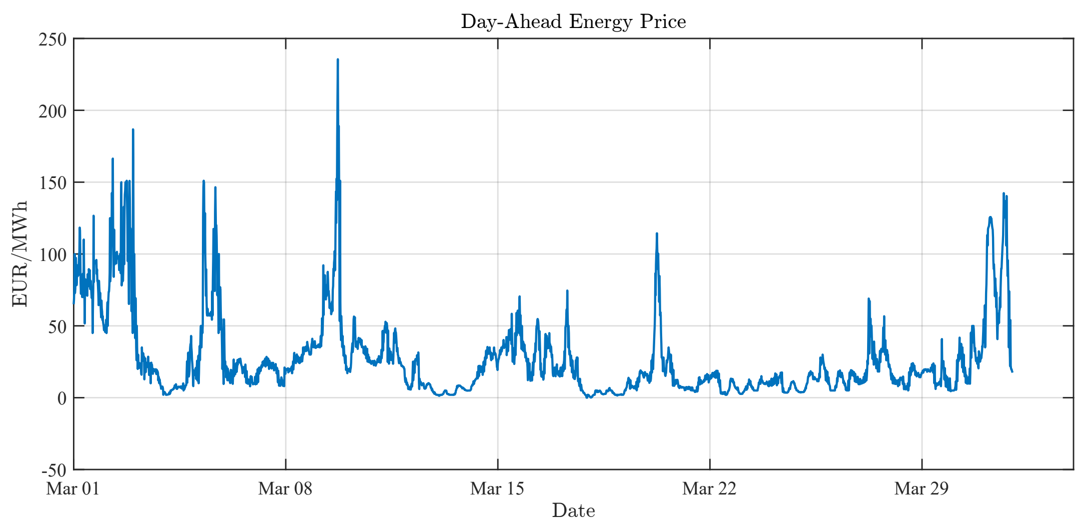

Figure 17: Day-ahead energy price used as the hourly energy-market revenue term λ_t^E in the bidding formulation.

The reserve price in Fig. 16 defines the capacity value used in the reserve-bidding and settlement assessment, whereas the energy price in Fig. 17 represents the opportunity cost of withholding wind power through deloaded operation. Therefore, the bidding decision depends on the trade-off between energy revenue and reserve-capacity value. When the naive strategy uses the full theoretical reserve, the offered reserve may exceed the effective reserve obtained from the RTDS simulations. In that case, the shortfall variable s_t^R captures the non-delivered reserve. In contrast, the η-aware strategy directly limits the offer through $R_t^{\mathrm{bid}} \leq \eta_{R,8s} R_t^{\mathrm{th}}$ reducing the risk of offering reserve that cannot be physically transferred to the PCC.

5.4.2 Bidding Outcomes

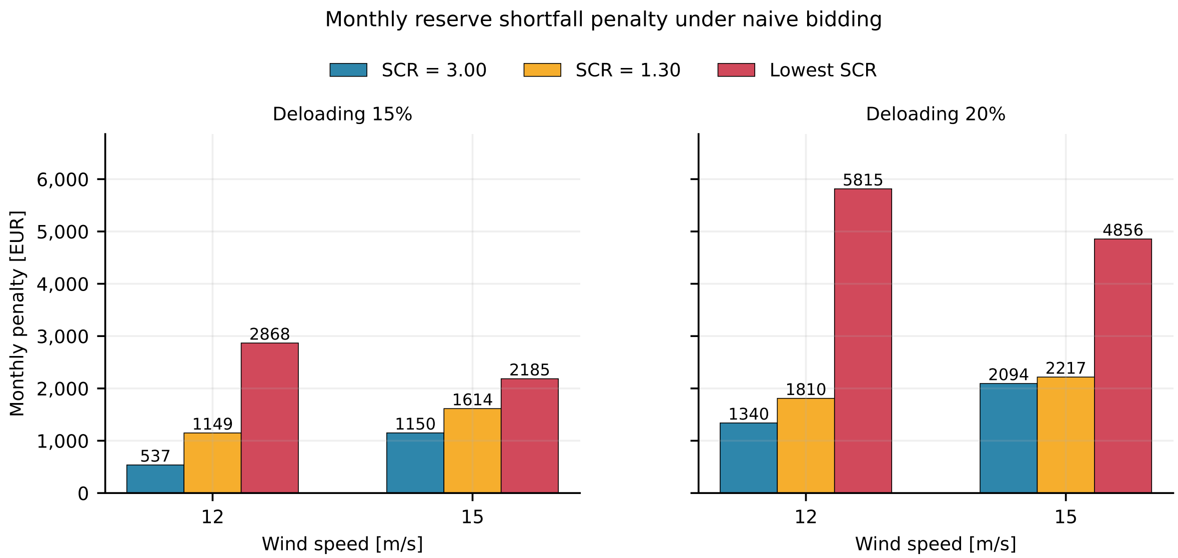

Figure 18: Monthly reserve shortfall penalty obtained for the naive strategy using the March 2026 market data. The bars are grouped by deloading level and wind speed, while the colors indicate the SCR cases considered in the reserve-deliverability assessment.

Fig. 18 shows the economic consequence of offering reserve according to the theoretical headroom without accounting for the delivered reserve ratio. For both deloading levels, the monthly shortfall penalty increases as the SCR decreases. This behavior is expected because the lowest-SCR cases exhibit the largest difference between the reserve offered by the naive strategy and the reserve effectively delivered at the PCC. For 15% deloading, the lowest-SCR penalty reaches 2868 EUR at 12 m/s and 2185 EUR at 15 m/s. For 20% deloading, the penalty exposure becomes more severe, reaching 5815 EUR at 12 m/s and 4856 EUR at 15 m/s. Thus, the economic risk of naive bidding is governed by the delivered-reserve ratio reported in Fig. 14, not only by the theoretical deloading headroom.

These results confirm that the market impact of reserve non-delivery is not determined only by the selected deloading level. It also depends on the operating point and on the ability of the plant to transfer the released reserve to the grid. Even though a larger deloading margin creates more theoretical reserve, it also increases the amount of capacity that can be overcommitted when the physical deliverability is limited. Therefore, the naive strategy exposes the plant to unnecessary shortfall penalties, especially under weak-grid conditions. The result supports the use of the η-aware strategy, where the reserve offer is derated through $\eta_{R,8s}$ before market participation.

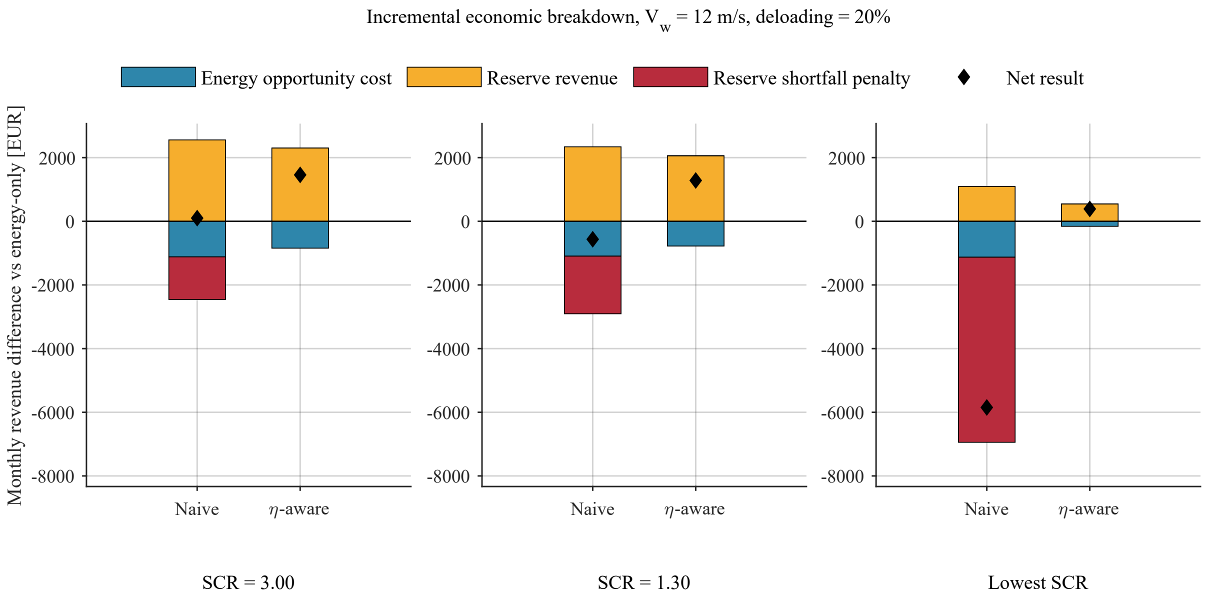

Figure 19: Incremental economic breakdown relative to the energy-only strategy for the representative operating point $V_w = 12\ \mathrm{m/s}$ and 20% deloading. The stacked bars show the energy opportunity cost, FCR-D Up reserve revenue, and reserve shortfall penalty, while the black diamond indicates the resulting net monthly difference.

Fig. 19 complements the monthly penalty results by decomposing the net economic effect of reserve participation into its main components. The negative energy component represents the opportunity cost of withholding active power from the energy market in order to create reserve headroom. The positive reserve component corresponds to the FCR-D Up capacity revenue, whereas the negative penalty component appears when the offered reserve exceeds the reserve effectively delivered at the PCC. For SCR = 3.00, the naive strategy remains almost neutral because the reserve revenue is largely offset by the energy opportunity cost and the shortfall penalty. For SCR = 1.30, the naive strategy becomes slightly uneconomic, while the η-aware strategy remains profitable by limiting the offered reserve according to $\eta_{R,8s}$. Under the lowest-SCR condition, the naive strategy becomes strongly detrimental because the penalty dominates the reserve revenue, whereas the η-aware strategy remains slightly positive despite the reduced physically deliverable reserve. This confirms that including the delivered reserve ratio in the bidding decision prevents naive bids from becoming economically detrimental under weak-grid conditions.

Table 10: Incremental economic breakdown relative to the energy-only strategy for the representative operating point $V_w = 12\ \mathrm{m/s}$ and 20% deloading.

SCR case	Strategy	ΔE [EUR]	Reserve revenue [EUR]	Shortfall penalty [EUR]	ΔJ [EUR]
SCR = 3.00	Naive	-1118	2557	1340	99
SCR = 3.00	η-aware	-845	2302	0	1458
SCR = 1.30	Naive	-1095	2340	1810	-565
SCR = 1.30	η-aware	-778	2059	0	1281
Lowest SCR	Naive	-1129	1095	5815	-5849
Lowest SCR	η-aware	-159	546	0	388

Table 10 gives the numerical values represented in Fig. 19. For SCR = 3.00, the naive strategy is almost economically neutral: the reserve revenue of 2557 EUR compensates the energy opportunity cost of 1118

EUR, but the remaining shortfall penalty of 1340 EUR reduces the monthly gain to only 99 EUR. In the same grid condition, the η-aware strategy reduces the reserve revenue to 2302 EUR because it offers only the deliverable reserve, but it also removes the penalty term; therefore, the net monthly increment increases to 1458 EUR. This means that even in the strongest grid case shown in Fig. 19, bidding the full theoretical headroom is not the best option once non-delivery is penalized.

For SCR = 1.30, the same mechanism becomes more evident. The naive strategy still receives 2340 EUR in reserve revenue, but the 1810 EUR shortfall penalty is larger than the margin left after the energy opportunity cost, producing a negative net result of -565 EUR. By contrast, the η-aware strategy accepts a lower reserve revenue of 2059 EUR, avoids the shortfall penalty, and obtains a positive monthly increment of 1281 EUR. In the lowest-SCR case, the difference is decisive: the naive strategy receives only 1095 EUR of reserve revenue while accumulating a 5815 EUR penalty, so the net result falls to -5849 EUR. The η-aware strategy limits the bid strongly, which lowers both the energy opportunity cost and the reserve revenue, but keeps the penalty at zero and preserves a positive result of 388 EUR. Therefore, the values in Table 10 explain the trend observed in Fig. 19: as the grid becomes weaker, the economic loss is driven mainly by reserve overcommitment, not by the energy opportunity cost itself. Values are rounded to the nearest EUR; therefore, row totals may differ slightly from the sum of rounded components.

Table 11: Incremental economic breakdown relative to the energy-only strategy for the representative operating point $V_w = 15$ m/s and 20% deloading.

SCR case	Strategy	ΔE [EUR]	Reserve revenue [EUR]	Shortfall penalty [EUR]	ΔJ [EUR]
SCR = 3.00	Naive	-1118	2305	2094	-906
SCR = 3.00	η-aware	-753	1989	0	1236
SCR = 1.30	Naive	-1050	2084	2217	-1184
SCR = 1.30	η-aware	-603	1694	0	1091
Lowest SCR	Naive	-1134	1430	4856	-4561
Lowest SCR	η-aware	-348	927	0	580

Table 11 extends the economic comparison to the $V_w = 15$ m/s operating point with 20% deloading. In this case, the naive strategy produces a negative net increment for all SCR conditions. For SCR = 3.00, the reserve revenue of 2305 EUR is not sufficient to compensate the 1118 EUR energy opportunity cost and the 2094 EUR shortfall penalty, leading to a net result of -906 EUR. For SCR = 1.30, the same mechanism produces a net loss of -1184 EUR. Under the lowest-SCR condition, the penalty increases to 4856 EUR and the net loss reaches -4561 EUR.

In contrast, the η-aware strategy remains economically positive in the three grid-strength conditions because it limits the reserve bid according to the physically deliverable reserve reported in Fig. 14. This eliminates the shortfall penalty and yields positive net increments of 1236 EUR, 1091 EUR, and 580 EUR for SCR = 3.00, SCR = 1.30, and the lowest-SCR case, respectively. Values are rounded to the nearest EUR; therefore, row totals may differ slightly from the sum of rounded components. Since Fig. 19 already shows the stacked-component interpretation for the 12 m/s representative case, an additional figure for 15 m/s is not included; Table 11 provides the full numerical decomposition without duplicating the same visual structure. Accordingly, the absolute monetary outcomes are scenario-dependent, whereas the comparison between bidding strategies is the main result of the assessment.

Overall, the results show that incorporating the delivered reserve ratio into the bidding strategy consistently reduces the economic impact of reserve shortfalls under the analyzed operating conditions. While the absolute monthly economic outcomes depend on the selected market period, reserve prices, and penalty assumptions, the consistent ranking of the evaluated strategies indicates that accounting for physically deliverable reserve improves the robustness of reserve bidding under weak-grid conditions.

6 Conclusions

This work assessed the impact of weak-grid conditions on the reserve deliverability of a DFIG-based wind power plant and its implications for reserve-market participation. The results show that estimating reserve capability only from the available active-power headroom can significantly overestimate the actual reserve delivered at the PCC. Under weak-grid conditions, the interaction between active-power injection, voltage support, converter current limits, and grid impedance reduces the effective active-power response of the wind power plant.

The EMT simulations showed that the delivered reserve ratio, $\eta_{R,8s}$, decreases as the SCR is reduced. In the most restrictive cases, the delivered reserve reached only about 36.10% of the theoretical headroom. This confirms that the headroom available at the turbine or plant control level is not necessarily equivalent to the active-power reserve that can be effectively delivered to the grid. Therefore, weak-grid constraints must be included when estimating the reserve capability of DFIG-based wind power plants.

These findings also highlight the methodological contribution of the RSCAD/RTDS-based EMT assessment. While steady-state power-flow calculations or analytical capability curves can provide an initial estimate of the available active-power headroom, they do not capture the dynamic interactions that determine how much of that headroom is effectively transferred to the grid. In particular, the delivered response depends on the combined behavior of the converter controls, the PLL, the current limits and current-priority logic, the PCC-voltage dynamics, the dc-link regulation, and the electromechanical response of the rotor. Although RMS models can represent the slower system dynamics, their representation of fast control interactions and limiter transitions depends on the adopted simplifications. The EMT implementation therefore made it possible to quantify, in the time domain, when part of the theoretical reserve was temporarily used for voltage support or rotor acceleration instead of being delivered as active power at the PCC. This assessment provided the physical basis for the delivered reserve ratio $\eta_{R,8s}$ subsequently used in the economic analysis.

Using the EMT-derived delivered reserve ratio in the economic evaluation, the results show that the naive strategy can become economically unfavorable as the grid weakens. For the representative case with $V_w = 12\ \mathrm{m/s}$ and 20% deloading, the naive strategy obtained a net incremental result of 99 EUR at SCR = 3.00. However, the corresponding result decreased to -565 EUR at SCR = 1.30 and to -5849 EUR in the lowest-SCR case. In contrast, the η-aware strategy remained profitable in all cases, with net incremental results of 1458 EUR, 1281 EUR, and 388 EUR, respectively. Therefore, including the delivered reserve ratio changed the market outcome from severe economic losses to positive net results under weak-grid conditions.

A similar trend was observed for $V_w = 15\ \mathrm{m/s}$ and 20% deloading. The naive strategy produced negative net incremental results for all SCR levels, with -906 EUR at SCR = 3.00, -1184 EUR at SCR = 1.30, and -4561 EUR in the lowest-SCR case. Meanwhile, the η-aware strategy achieved positive results of 1236 EUR, 1091 EUR, and 580 EUR, respectively. These results show that maximizing the reserve volume offered to the market is not necessarily the best economic decision. Instead, the reserve bid should be limited according to the amount of active power that can actually be delivered at the PCC.

The comparison among the energy-only, naive, and η-aware strategies demonstrates that reserve provision can be economically attractive only when the bid reflects the physical deliverability limits of the wind power plant. Otherwise, additional reserve revenue can be outweighed by shortfall penalties, especially in very weak grids. Therefore, the economic assessment shows that limiting the reserve bid using $\eta_{R,8s}$ provides a more realistic representation of the plant capability and reduces its exposure to shortfall penalties.

Overall, the study shows that weak-grid effects are not only a technical constraint but also an economic risk for DFIG-based wind power plants participating in ancillary-service markets. Considering PCC-level reserve deliverability in the economic assessment reduces exposure to penalties, improves the expected market outcome, and provides a more reliable estimate of the reserve contribution that the plant can actually deliver to the power system.

6.1 Limitations and Future Work

The reserve-deliverability results were obtained for a limited set of wind speeds, deloading levels, SCR values, and one frequency disturbance. Therefore, the factor $\eta_{R,8s}$ should be interpreted as a scenario-dependent metric rather than as a universal parameter of the wind power plant. Its value also depends on the adopted DFIG model, PLL tuning, converter current limits, current-priority logic, grid equivalent, and the selected 8 s evaluation window.

The reserve-bidding formulation represents an offline, scenario-based economic assessment using deterministic energy and reserve prices and a simplified shortfall penalty. It does not reproduce the complete market-clearing process or explicitly consider competition among market participants, strategic bidding, wind-speed uncertainty, operating-point uncertainty, price uncertainty, or reserve-activation uncertainty. Therefore, the proposed bidding model should not be interpreted as a complete commercial strategy, but as an assessment of how physical reserve-deliverability limitations affect the economic outcome of reserve participation.

Future work should extend the EMT analysis to additional operating conditions and grid-support functions, including low-voltage ride-through, synthetic-inertia response, different frequency disturbances, and alternative converter-control and current-priority strategies. The economic formulation could also be extended by modeling the stochastic behavior of wind speed, operating points, energy and reserve prices, and reserve activation. Finally, a complete market model including competition among participants, market clearing, strategic bidding, and settlement rules could be developed to evaluate the commercial performance of the evaluated η-aware strategy under more realistic conditions.

Annex A Power-System Parameterization Used in RSCAD

The following tables summarize the numerical data used to implement the complete power-system model shown in Fig. 5. They are included in the annex because they correspond to implementation parameters rather than to the conceptual description of the plant connection. The DFIG-based wind power plant considered in the reserve-deliverability study is connected at the Malleco bus; the buses listed in the following parameterization tables correspond to other aggregated system elements used to represent the surrounding network.

Table 12: Grid-forming (GFM) unit parameters

Type	f_{nom} [Hz]	H_{eq} [s]	V_B [kV]	K_p	K_q	S_{nom} [MVA]	Power factor	Bus	P_{set} [MW]	Q_{set} [Mvar]
GFM	50	3.6126	500	0.0433	0.0433	1300.5200	0.9055	NvaMaitencillo	900	0.1
GFM	50	5.1583	500	0.0888	0.0492	2747.5400	0.8800	Alto Jahuel	1280	0.1
GFM	50	4.6296	500	0.0731	0.0483	2168.3960	0.9179	Ancoa	900	0.1
GFM	50	4.9356	500	0.0642	0.0495	1973.8800	0.8855	Concepción	1000	0.1
GFM	50	5.8070	500	0.0128	0.0500	398.1900	0.8741	Mulchen	280	0.1

Table 13: Synchronous generator parameters

Type	f_{nom} [Hz]	H_{eq} [s]	V_B [kV]	P_0 [MW]	Q_0 [Mvar]	S_{nom} [MVA]	Power factor	Bus
SynGen	50	3.6380	220	140.0	188.527	234.824	0.8933	Lagunas
SynGen	50	4.9780	500	1940.0	4761.93	4846.23	0.8955	Kimal500
SynGen	50	3.9215	500	600.0	562.0436	689.85	0.8929	Cumbres
SynGen	50	5.2000	500	1600.0	3315.41	3388.5	0.8872	Quillota
SynGen	50	4.9786	500	1600.0	2664.59	2782.09	0.9319	Charrua
SynGen	50	3.1520	500	600.0	866.8348	917.2800	0.9052	Pichirropulli

Table 14: Demand modeled as grid-following load

Name	f_{nom} [Hz]	P_{nom} [MW]	V_B [kV]	Demand [MW]
PzoAlmonte	50	2441.6	220.0	156×2
Kimal220	50	258.537103	220.0	$(523 + 258) = 781 \times 2$
Changos	50	538.346245	500.0	538×2
Nva Cardones	50	382.569458	500.0	382×2
Polpaico	50	818.155396	500.0	818×2
Rapel	50	504.965509	500.0	505×2
Candelaria	50	404.986921	500.0	404×2
Ancoa	50	854.154231	500.0	743×2
Concepción	50	366.533617	500.0	366×2
Mulchen	50	227.447198	500.0	237×2
Pichirropulli	50	526.892074	500.0	514×2
Total demand				$5444 \times 2 = 10\,888$

Annex B Calculation of the SCR and the Grid Impedance Angle

The SCR is defined as the ratio between the three-phase short-circuit power at the point of connection and the rated power of the plant:

$$\mathrm{SCR} = \frac{S_{sc}}{S_{\text{rated}}} \tag{B.72}$$

By modeling the equivalent grid through a Thevenin impedance:

$$Z_g = R_g + j\omega L_g, \qquad \omega = 2\pi f \tag{B.73}$$

its magnitude is given by:

$$|Z_g| = \sqrt{R_g^2 + (\omega L_g)^2} \tag{B.74}$$

Furthermore, the three-phase short-circuit power seen from a bus with line-to-line voltage V_{LL} is calculated as:

$$S_{sc} = \frac{V_{LL}^2}{|Z_g|} \tag{B.75}$$

Annex C Wind Power Plant Model Parameters

The parameters used to represent the DFIG system are summarized in this section. First, the electrical and mechanical parameters of the machine are presented, followed by the control parameters associated with the converter controllers and the frequency support scheme.

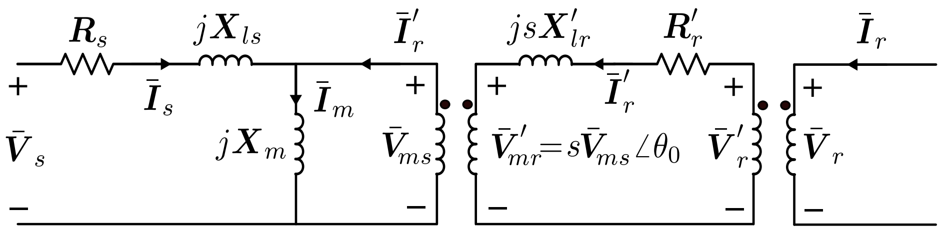

Figure 20: Steady-state per-phase equivalent circuit of the DFIG.

Table 15: Parameters of the DFIG Machine

Symbol	Description	Value
S_{nom}	Rated apparent power	25 MVA
$V_{LL,s}^{\text{nom}}$	Rated stator line-to-line voltage RMS	0.69 kV
f_s	Grid frequency	50 Hz
U_{dc}	DC-link voltage	1.2 kV
V_{rn}	Rated rotor line-to-line voltage RMS	1.82 kV
a	Rotor/stator turns ratio	2.6377
$I_{r\,\max}$	Maximum rotor current	1.2 pu
$I_{g\,\max}$	Maximum grid-side current	0.8 pu
R_s	Stator resistance	0.01 pu
R'_r	Rotor resistance referred to stator	0.006 pu
X_{ls}	Stator leakage reactance	0.102 pu
X'_{lr}	Rotor leakage reactance referred to stator	0.08596 pu
X_m	Magnetizing reactance	4.348 pu
C_{dc}	DC bus capacitor	10000 μF
H	Machine inertia constant	1.5 MWs/MVA
ω_s	Angular speed	100π rad/s

Table 16: PI Controller Parameters

Controller Set	**Associated PIs**	K_p	T_i [ms]
RSC outer-loop control	PI1, PI2	0.1	20.0
RSC inner current control	PI3, PI4	0.5	40.0
GSC outer-loop control	PI5, PI6	2.0	10.0
GSC d-axis current control	PI7	1.5	20.0
GSC q-axis current control	PI8	1.0	20.0
Phase-Locked Loop	PLL	30.0	5.0

Table 17: Parameters of the frequency control scheme

Symbol	Description	Value
K_1	Frequency control gain	17.0
K_2	Frequency control gain	150.0
R_ω	Rotor-speed regulation coefficient	0.05
R_β	Scheduled pitch-angle regulation coefficient	Table 19
Δf_{sat}	Full-reserve activation threshold	0.01 pu

Table 18: Pitch-control parameters

Symbol	Description	Value
T_β	Pitch actuator time constant	3 s
β_{min}	Minimum pitch angle	$0°$
β_{max}	Maximum pitch angle	$36°$
$\dot{\beta}_{\text{min}}$	Minimum pitch-rate limit	$-10°/\text{s}$
$\dot{\beta}_{\text{max}}$	Maximum pitch-rate limit	$10°/\text{s}$
$K_{p,\omega}$	Rotor-speed pitch correction proportional gain	0.2
$T_{i,\omega}$	Rotor-speed pitch correction integral time constant	0.1 s

Table 19: R_β values for the simulated pitch-regulated cases

V_w (m/s)	Deloading	β_0 (°)	β_{ND} (°)	$\Delta\beta_{\text{max}}$ (°)	R_β (pu/°)
12	20%	2.687	0.000	2.687	0.00372
12	15%	1.689	0.000	1.689	0.00592
15	20%	13.984	9.854	4.130	0.00242
15	15%	13.063	9.854	3.209	0.00312

Annex D Dynamic Performance Index and PCC Selection

The selection of the PCC was additionally supported by the Dynamic Performance Index (IDD) used in the Chilean technical framework for system robustness assessment. According to the Technical Standard for Security and Quality of Service, the IDD at bus j is defined as the area between the pre-fault RMS voltage and the transient RMS-voltage trajectory at the same bus [48]. In this work, the indicator was evaluated as

$$IDD_j = \int_{t_f}^{t_{ff}} |v_j(t) - v_{j,0}|\, dt, \tag{D.76}$$

where $v_j(t)$ is the RMS voltage at bus j, $v_{j,0}$ is the pre-fault RMS voltage, t_f is the fault inception time, and t_{ff} is the final time used for the transient-performance evaluation. Therefore, a larger IDD indicates a larger accumulated voltage deviation, either because the voltage excursion is deeper, because the recovery is slower, or because both effects occur simultaneously.

The current version of the robustness methodology establishes that the IDD calculated at the bus closest to the fault location must satisfy $IDD_j < 0.16$, where 0.16 is defined as the worst admissible value for the robustness study [48]. This value is therefore interpreted here as a system-robustness assessment threshold, not as a direct connection-admissibility requirement for a specific generation plant. In addition, the measures derived from the robustness study are not binding by themselves and do not directly impose operational restrictions on converter-based generation units; rather, the study is used as a technical input for planning, operation, and complementary-service assessments [48]. The IDD values obtained for the analyzed network are summarized in Tables 20 and 21, separated according to the 220 kV and 500 kV subsystems and ordered from the smallest to the largest value.

Table 20: IDD values for the 220 kV subsystem, ordered from smallest to largest.

Bus	IDD
Changos 220	0.047691
Lagunas	0.072667
Zaldivar	0.195927
Parinacota	0.220564
Pozo Almonte	0.587754
Kimal 220	1.541467

Table 21: IDD values for the 500 kV subsystem, ordered from smallest to largest.

Bus	IDD
Maitencillo	0.047691
Polpaico	0.072667
Rapel	0.113019
Candelaria	0.115143
Cardones	0.115143
Kimal 500	0.127120
Pichirropulli	0.127120
Charrua	0.133412
Pto. Montt	0.133412
Alto Jahuel	0.134240
Ancud	0.135813
Quillota	0.136079
Changos 500	0.144009
Pan de Azucar	0.144009
Ancoa	0.147248
Concepcion	0.195927
Cumbres	0.220564
Mulchen	0.364248
Malleco	0.587754
Parinas	1.541467

The DFIG-based wind power plant was connected at the Malleco bus because the objective was to study reserve delivery in a weak area of the system, rather than at a very strong bus where the effect of grid weakness would be less visible. Malleco presents a relatively high IDD within the 500 kV subsystem, indicating a significant transient-voltage deviation and therefore a suitable location to stress the interaction between PCC-voltage dynamics, converter-current limits, and active-power transfer. At the same time, it was not the most severe bus in the system: Parinas and Kimal 220 exhibit substantially higher IDD values. Thus, Malleco provided a weak-grid location with a large dynamic-performance index, but without selecting the most extreme condition that could lead to immediate system collapse or make the reserve-delivery analysis dominated only by instability.

It should also be noted that the PCC selection was made before the recently updated robustness methodology explicitly provided the $IDD_j < 0.16$ threshold. Under the current robustness-study criterion, the Malleco value reported in Table 21 exceeds this threshold. However, this should not be interpreted as an automatic prohibition for an existing or hypothetical wind power plant connection at that bus. Instead, it indicates that Malleco belongs to a dynamically demanding area where voltage deviations following short-circuit events are significant and where additional robustness measures or operational assessments may be required. In the context of this work, this is consistent with the purpose of selecting a weak-grid location to evaluate how reserve deliverability deteriorates when the wind power plant is connected to a dynamically stressed area of the network.

Annex E Exploratory Active-Power Transfer under Constant Power Factor

Fig. 21 is used as the reference diagram for this derivation. A motor-reference convention is adopted: negative active power denotes generation, and negative reactive power denotes reactive-power injection into the grid. In addition, the d-axis of the synchronous reference frame is aligned with the stator voltage, so that $V_{sq} = 0$.

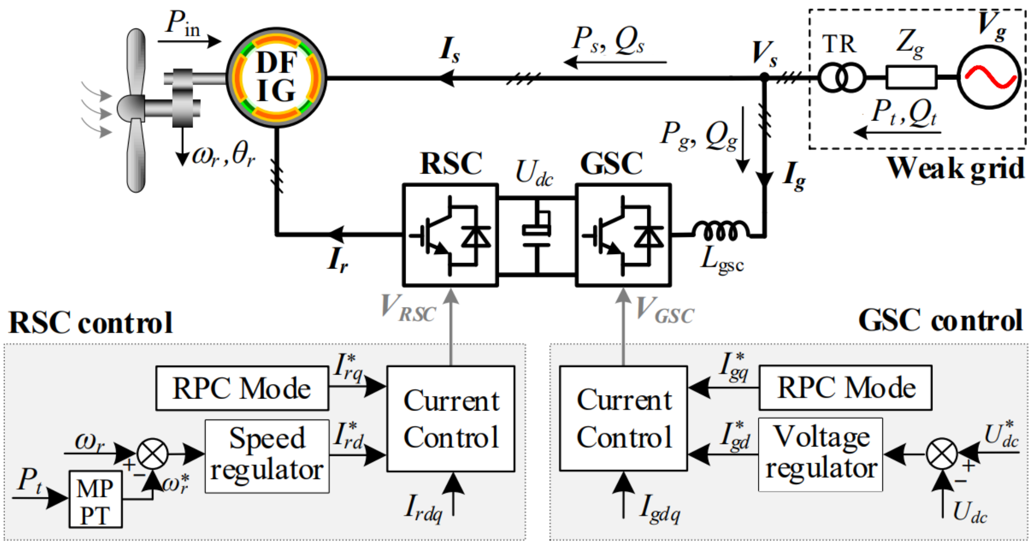

Figure 21: DFIG connected to a weak grid through an equivalent grid impedance, including the RSC, GSC, PCC, and adopted current and power-flow conventions.

The objective of this annex is to obtain an explicit expression for the active power transferred to the grid as a function of the power angle δ_g, the slip s, and the power-factor angles φ_1 and φ_2. The derivation follows the weak-grid power-transfer framework used in [5], while keeping the notation consistent with the rest of this work.

This analysis is included as an exploratory extension because the main study uses constant-voltage control during reserve delivery. This choice is consistent with contingency-oriented operation, where voltage regulation at the PCC is typically prioritized in grid-code compliance studies. The constant-power-factor case is therefore not used as the main control architecture of the work, but it is useful to show how active-power transfer changes when the stator and GSC power factors are imposed instead of allowing the controller to regulate voltage.

DFIG Model and Network Equations

The electromagnetic DFIG model, written in space-vector form, is

$$\begin{cases} \boldsymbol{v}_s = -R_s\boldsymbol{i}_s + j\omega_s\boldsymbol{\psi}_s + \dfrac{d\boldsymbol{\psi}_s}{dt}, \\ \boldsymbol{v}_r = R_r\boldsymbol{i}_r + j\omega_r\boldsymbol{\psi}_r + \dfrac{d\boldsymbol{\psi}_r}{dt}, \\ \boldsymbol{\psi}_s = -L_s\boldsymbol{i}_s + L_m\boldsymbol{i}_r, \\ \boldsymbol{\psi}_r = -L_m\boldsymbol{i}_s + L_r\boldsymbol{i}_r. \end{cases} \tag{E.77}$$

The weak grid is represented by the equivalent impedance $Z_g = R_g + jX_g$ between the PCC and the grid voltage source $\boldsymbol{v}_g$. Under the adopted current references, namely grid $\to$ PCC, PCC $\to$ stator, and PCC $\to$ GSC, the KVL between the stator voltage and the grid voltage is

$$\boldsymbol{v}_s - \boldsymbol{v}_g = (R_g + jX_g)\,\boldsymbol{i}_t, \tag{E.78}$$

where the total current at the PCC satisfies the KCL

$$\boldsymbol{i}_t = \boldsymbol{i}_s + \boldsymbol{i}_g. \tag{E.79}$$

Aligning the d-axis with $\boldsymbol{v}_s$ gives $V_{sq} = 0$. Separating (E.78) into dq components gives

$$\begin{aligned} V_{sd} &= V_{gd} + R_g I_{td} - X_g I_{tq}, \\ 0 &= V_{gq} + R_g I_{tq} + X_g I_{td}. \end{aligned} \tag{E.80}$$

Phasor Relations and Angle Definitions

To construct the weak-grid DFIG phasor diagram, the power angle is defined as the angular difference between V_s and V_g:

$$\delta_g = \theta_{V_s} - \theta_{V_g} = 0 - \theta_{V_g} = -\theta_{V_g}. \tag{E.81}$$

The angles φ_1 and φ_2 represent the stator-side and GSC-side power-factor angles, respectively, both referred to V_s. With $\theta_{V_s} = 0$,

$$\tan(\varphi_1) = \tan(\theta_{V_s} - \theta_{I_s}) = \tan(-\theta_{I_s}) = \frac{-I_{sq}}{I_{sd}}, \tag{E.82}$$

$$\tan(\varphi_2) = \tan(\theta_{V_s} - \theta_{I_g}) = \tan(-\theta_{I_g}) = \frac{-I_{gq}}{I_{gd}}. \tag{E.83}$$

From (E.81), the grid-voltage components are parameterized as

$$V_{gd} = V_g \cos\delta_g, \qquad V_{gq} = V_g \sin(\theta_{V_g}) = V_g \sin(-\delta_g) = -V_g \sin\delta_g. \tag{E.84}$$

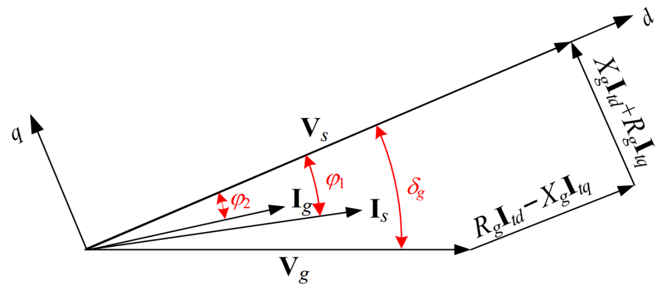

Figure 22: Phasor diagram used to define the stator-voltage reference, grid-voltage angle, current components, and power-factor angles.

Substituting (E.84) into (E.80) and using the KCL in (E.79), the q-axis equation can be written as

$$V_g \sin\delta_g = X_g I_{td} + R_g I_{tq} = X_g\left(I_{sd} + I_{gd}\right) + R_g\left(I_{sq} + I_{gq}\right). \tag{E.85}$$

The d-axis component leads to

$$\begin{cases} V_{sd} = V_g \cos\delta_g + R_g I_{td} - X_g I_{tq} \\ \quad\;\; = V_g \cos\delta_g + R_g\left(I_{sd} + I_{gd}\right) - X_g\left(I_{sq} + I_{gq}\right), \\ V_{sq} = 0. \end{cases} \tag{E.86}$$

Current Relations Through Slip

To express the currents as a function of slip, the power sharing between stator and rotor is written under the adopted convention and without chopper activation. The input mechanical power P_{in} is considered positive into the machine, whereas negative electrical active power corresponds to DFIG generation. Under these assumptions,

$$P_s = \frac{-P_{in}}{1-s}, \tag{E.87}$$

$$P_r = \frac{s\,P_{in}}{1-s}. \tag{E.88}$$

Neglecting converter losses and without chopper activation, the GSC active power is equal to the rotor active power:

$$P_g = P_r = -s\,P_s. \tag{E.89}$$

The total active power exchanged at the PCC is therefore

$$P_t = P_s + P_g = \frac{-P_{in}}{1-s} + \frac{s\,P_{in}}{1-s} = -P_{in} = P_s(1-s). \tag{E.90}$$

Since $V_{sq} = 0$, the stator and GSC active powers can be written in terms of the d-axis currents:

$$P_s = \frac{3}{2} V_{sd}\, I_{sd}, \tag{E.91}$$

$$P_g = \frac{3}{2} V_{sd}\, I_{gd}. \tag{E.92}$$

Substituting (E.91) and (E.92) into (E.89) gives

$$I_{gd} = -s\, I_{sd}. \tag{E.93}$$

Additionally, (E.82)–(E.83) give

$$I_{sq} = -I_{sd} \tan\varphi_1, \qquad I_{gq} = -I_{gd} \tan\varphi_2 = s\, I_{sd} \tan\varphi_2. \tag{E.94}$$

Using (E.93) and (E.94), (E.85) is fully parameterized by I_{sd}:

$$V_g \sin\delta_g = I_{sd} \Big[X_g(1-s) + R_g \left(\tan\varphi_1 - s \tan\varphi_2 \right) \Big]. \tag{E.95}$$

Defining the common denominator

$$D = X_g(1-s) + R_g \left(\tan\varphi_1 - s \tan\varphi_2 \right), \tag{E.96}$$

one obtains

$$I_{sd} = \frac{V_g \sin\delta_g}{D}, \tag{E.97}$$

$$I_{sq} = \frac{-V_g \sin\delta_g\, \tan\varphi_1}{D}, \tag{E.98}$$

$$I_{gd} = \frac{-s\, V_g \sin\delta_g}{D}, \tag{E.99}$$

$$I_{gq} = \frac{s\, V_g \sin\delta_g\, \tan\varphi_2}{D}. \tag{E.100}$$

Finally, substituting (E.97)–(E.100) into (E.86) and factoring $V_g \sin\delta_g$ gives

$$V_{sd} = V_g \cos\delta_g + V_g \sin\delta_g\, \frac{R_g(1-s) + X_g \left(\tan\varphi_1 - s \tan\varphi_2 \right)}{D}. \tag{E.101}$$

Steady-State Rotor Currents

To obtain the rotor currents, the steady-state DFIG model in (E.77) is used. At this stage, steady-state operation is assumed, i.e., $d\boldsymbol{\psi}_s/dt = d\boldsymbol{\psi}_r/dt = 0$, and R_s (and R_r, when applicable) is neglected with respect to the reactive terms. Therefore,

$$\boldsymbol{v}_s \approx j\omega_s \boldsymbol{\psi}_s. \tag{E.102}$$

Separating into dq axes and considering $V_{sq} = 0$ gives

$$\begin{aligned} V_{sd} &= -\omega_s \psi_{sq}, \\ V_{sq} &= \omega_s \psi_{sd} = 0 \end{aligned} \qquad \Rightarrow \qquad \psi_{sd} = 0, \quad \psi_{sq} = -\frac{V_{sd}}{\omega_s}. \tag{E.103}$$

From the stator-flux equation

$$\boldsymbol{\psi}_s = -L_s \boldsymbol{i}_s + L_m \boldsymbol{i}_r, \tag{E.104}$$

the dq components are

$$\begin{aligned} \psi_{sd} &= -L_s I_{sd} + L_m I_{rd}, \\ \psi_{sq} &= -L_s I_{sq} + L_m I_{rq}. \end{aligned} \tag{E.105}$$

Substituting (E.103) into (E.105) and solving gives

$$I_{rd} = \frac{L_s}{L_m} I_{sd}, \tag{E.106}$$

$$I_{rq} = \frac{1}{L_m} \left(\psi_{sq} + L_s I_{sq} \right) = \frac{1}{L_m} \left(\frac{-V_{sd}}{\omega_s} + L_s I_{sq} \right). \tag{E.107}$$

Replacing (E.97), (E.98), and (E.101) gives

$$I_{rd} = \frac{L_s}{L_m} \frac{V_g \sin \delta_g}{D}, \tag{E.108}$$

$$I_{rq} = \frac{1}{L_m} \left(\frac{-1}{\omega_s} V_{sd} + L_s I_{sq} \right), \tag{E.109}$$

where V_{sd} and I_{sq} are substituted using (E.101) and (E.98), respectively, which leads to

$$I_{rq} = -\frac{V_g \cos \delta_g}{\omega_s L_m} - \frac{V_g \sin \delta_g}{D\, L_m} \left(\frac{R_g(1-s) + X_g \left(\tan \varphi_1 - s \tan \varphi_2 \right)}{\omega_s} + L_s \tan \varphi_1 \right). \tag{E.110}$$

Active and Reactive Power at the PCC

With $V_{sq} = 0$, the stator powers are

$$P_s = \frac{3}{2} V_{sd} I_{sd}, \qquad Q_s = -\frac{3}{2} V_{sd} I_{sq}. \tag{E.111}$$

Using (E.82), one obtains

$$Q_s = P_s \tan \varphi_1. \tag{E.112}$$

Substituting (E.97) and (E.101) into (E.111) gives

$$P_s = \frac{3}{2} \frac{V_g^2 \sin \delta_g}{D} \left(\cos \delta_g + \sin \delta_g \frac{R_g(1-s) + X_g \left(\tan \varphi_1 - s \tan \varphi_2 \right)}{D} \right). \tag{E.113}$$

At the PCC, the total active and reactive powers are

$$P_t = P_s + P_g, \qquad Q_t = Q_s + Q_g. \tag{E.114}$$

Since φ_1 and φ_2 represent the stator and GSC power-factor angles, respectively,

$$Q_s = P_s \tan \varphi_1, \qquad Q_g = P_g \tan \varphi_2. \tag{E.115}$$

Using $P_g = -sP_s$ from (E.89),

$$Q_g = (-sP_s) \tan \varphi_2. \tag{E.116}$$

Finally,

$$Q_t = Q_s + Q_g = P_s \tan \varphi_1 - sP_s \tan \varphi_2 = P_s \left(\tan \varphi_1 - s \tan \varphi_2 \right). \tag{E.117}$$

Sensitivity of Active Power with Respect to the Power Angle

To analyze the influence of δ_g on the transferred active power, P_t is differentiated with respect to that angle. For a weak grid dominated by reactance, $R_g \approx 0$ is considered. This assumption does not imply a strong grid; it represents a purely inductive case, which is conservative in terms of active-power transfer for a given SCR. Under $R_g \approx 0$, and using $D = X_g(1-s)$,

$$P_t = \frac{3V_g^2}{2X_g}\left[\sin\delta_g\cos\delta_g + \frac{\tan\varphi_1 - s\tan\varphi_2}{1-s}\sin^2\delta_g\right]. \tag{E.118}$$

Define

$$K = \frac{\tan\varphi_1 - s\tan\varphi_2}{1-s}. \tag{E.119}$$

Then,

$$P_t = \frac{3V_g^2}{2X_g}\left(\sin\delta_g\cos\delta_g + K\sin^2\delta_g\right). \tag{E.120}$$

Differentiating (E.118) with respect to δ_g gives

$$\frac{dP_t}{d\delta_g} = \frac{3V_g^2}{2X_g}\left[\frac{d}{d\delta_g}(\sin\delta_g\cos\delta_g) + K\frac{d}{d\delta_g}(\sin^2\delta_g)\right]. \tag{E.121}$$

Using

$$\frac{d}{d\delta}(\sin\delta\cos\delta) = \cos^2\delta - \sin^2\delta = \cos 2\delta, \qquad \frac{d}{d\delta}(\sin^2\delta) = 2\sin\delta\cos\delta = \sin 2\delta, \tag{E.122}$$

one obtains

$$\frac{dP_t}{d\delta_g} = \frac{3V_g^2}{2X_g}\left(K\sin 2\delta_g + \cos 2\delta_g\right). \tag{E.123}$$

Substituting (E.119),

$$\frac{dP_t}{d\delta_g} = \frac{3V_g^2}{2X_g}\left(\frac{\tan\varphi_1 - s\tan\varphi_2}{1-s}\sin 2\delta_g + \cos 2\delta_g\right). \tag{E.124}$$

The maximizing angle satisfies

$$\frac{dP_t}{d\delta_g} = 0. \tag{E.125}$$

From (E.123)–(E.125),

$$K\sin 2\delta_g + \cos 2\delta_g = 0 \qquad \Rightarrow \qquad \tan(2\delta_g) = -\frac{1}{K}. \tag{E.126}$$

Therefore, the optimal angle can be written as

$$\delta_{g\,\max} = \begin{cases} \dfrac{\pi}{2} - \dfrac{1}{2}\arctan\left(\dfrac{1}{K}\right), & K > 0, \\ \dfrac{\pi}{4}, & K = 0, \\ -\dfrac{1}{2}\arctan\left(\dfrac{1}{K}\right), & K < 0. \end{cases} \tag{E.127}$$

The maximum active power is obtained from

$$P_{t\,\max} = P_t(\delta_{g\,\max}). \tag{E.128}$$

Using

$$\sin\delta\cos\delta = \frac{1}{2}\sin(2\delta), \tag{E.129}$$

$$\sin^2\delta = \frac{1-\cos(2\delta)}{2}, \tag{E.130}$$

(E.120) becomes

$$P_t = \frac{3V_g^2}{4X_g}\left(\sin 2\delta_g + K - K\cos 2\delta_g\right). \tag{E.131}$$

At the optimum, $\cos 2\delta_{g\,\max} = -K\sin 2\delta_{g\,\max}$, and therefore

$$P_{t\,\max} = \frac{3V_g^2}{4X_g}\left((1+K^2)\sin 2\delta_{g\,\max} + K\right). \tag{E.132}$$

Since

$$\sin(2\delta_{g\,\max}) = \frac{1}{\sqrt{1+K^2}}, \tag{E.133}$$

the maximum active power becomes

$$P_{t\,\max} = \frac{3V_g^2}{4X_g}\left(\sqrt{1+K^2} + K\right). \tag{E.134}$$

Finally, since $R_g \approx 0 \Rightarrow |Z_g| \approx X_g$, the SCR can be expressed as

$$\mathrm{SCR} = \frac{S_{cc}}{P_n} = \frac{V_g^2}{P_n|Z_g|} \approx \frac{V_g^2}{P_n X_g} \qquad \Rightarrow \qquad \frac{V_g^2}{X_g} \approx P_n \cdot \mathrm{SCR}. \tag{E.135}$$

Replacing (E.119) and (E.135) in (E.134), and expressing $P_{t\,\max}$ in pu over P_n, gives

$$\frac{P_{t\,\max}}{P_n} = \frac{3}{4}\mathrm{SCR}\left(\sqrt{1+\left(\frac{\tan\varphi_1 - s\tan\varphi_2}{1-s}\right)^2} + \frac{\tan\varphi_1 - s\tan\varphi_2}{1-s}\right). \tag{E.136}$$

Equation (E.136) explicitly shows that the angle-based maximum transferable active power depends on the SCR and on the operating point through the slip s and the power-factor angles φ_1 and φ_2. However, this expression represents only the power-angle transfer limit. If the power-angle limit is not reached first, the DFIG may still be limited by the RSC or GSC current capacity, as discussed in [5]. This distinction is important for the exploratory constant-power-factor simulations reported next: for the adopted DFIG parameters, the theoretical angle limit does not necessarily predict curtailment, but the simulated response can still degrade because the converters reach their current limits.

Exploratory Simulation Results under Constant Power Factor

The following figures show the active-power response obtained when the DFIG is commanded to deliver 1 pu under constant power factor. In this convention, positive power factor denotes inductive operation and negative power factor denotes capacitive operation. Each figure compares inductive and capacitive operation for the same absolute power factor. The results show that the requested 1 pu active power can be maintained only above certain SCR values; as the grid becomes weaker, the transferred active power deteriorates. Since (E.136) does not predict an angle-based restriction for some of these operating points, the degradation is attributed to converter-current limitations rather than to the theoretical power-angle limit.

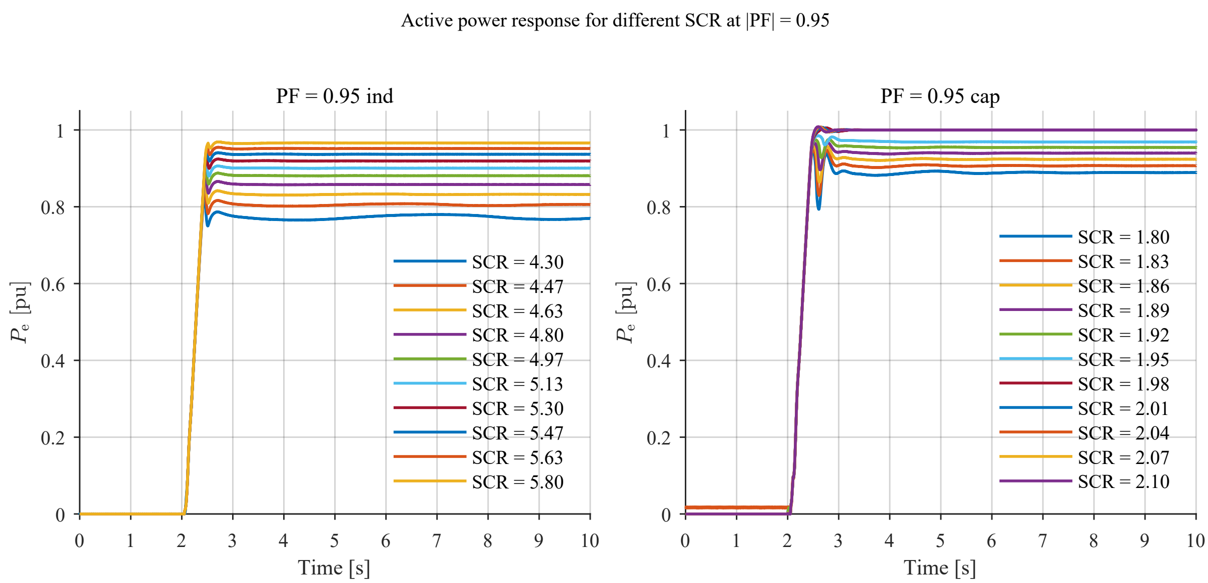

Figure 23: Active-power response under constant power factor for $|PF| = 0.95$, comparing inductive and capacitive operation for different SCR values.

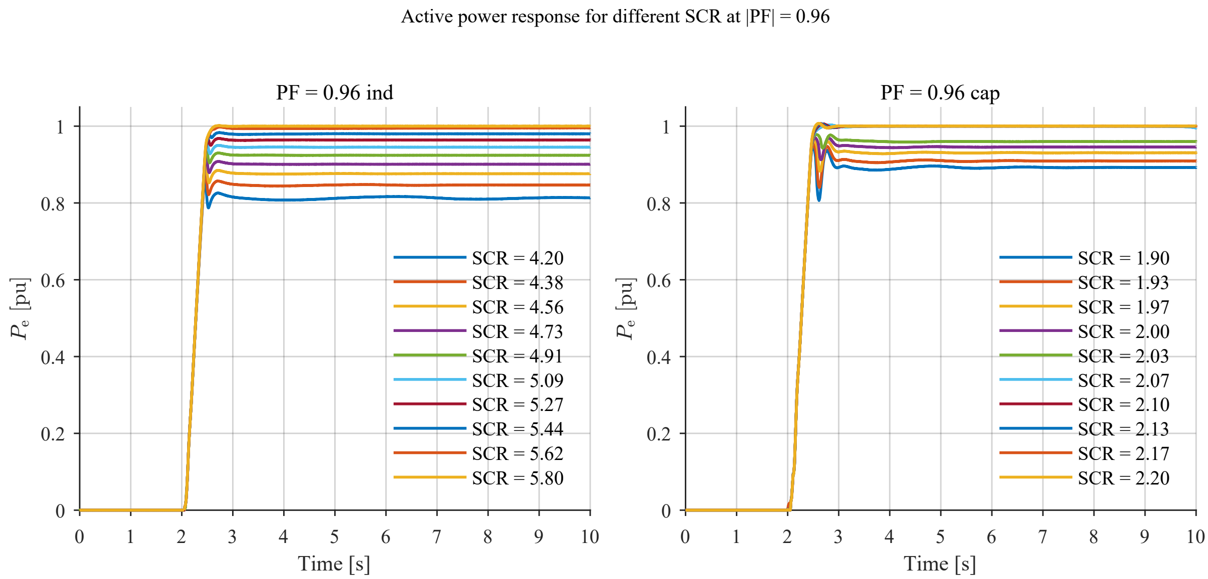

Figure 24: Active-power response under constant power factor for $|PF| = 0.96$, comparing inductive and capacitive operation for different SCR values.

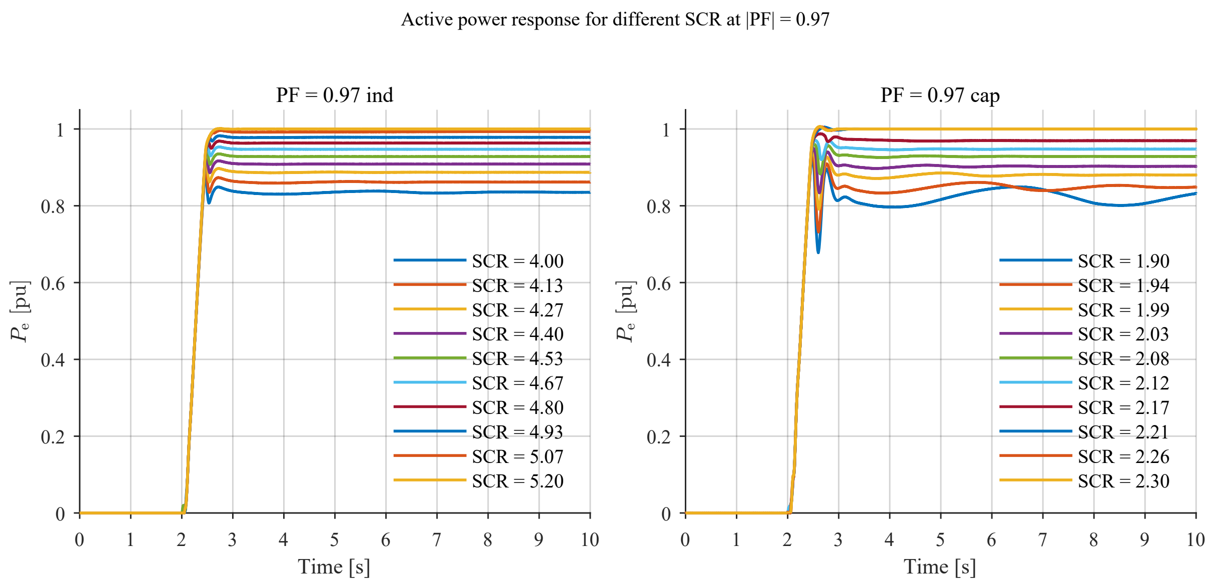

Figure 25: Active-power response under constant power factor for $|PF| = 0.97$, comparing inductive and capacitive operation for different SCR values.

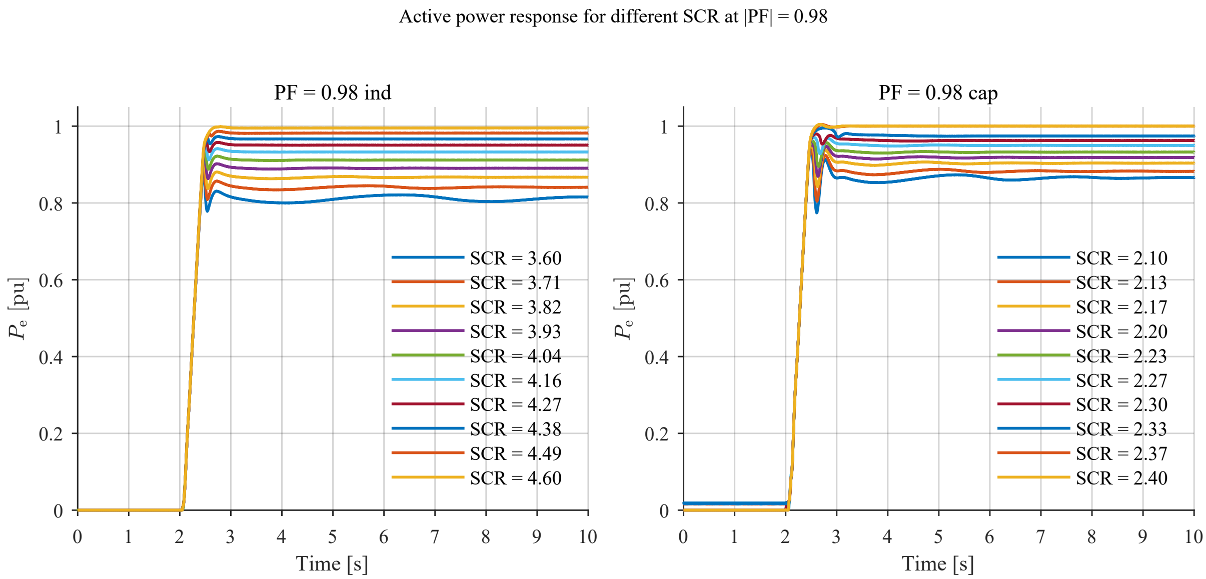

Figure 26: Active-power response under constant power factor for $|PF| = 0.98$, comparing inductive and capacitive operation for different SCR values.

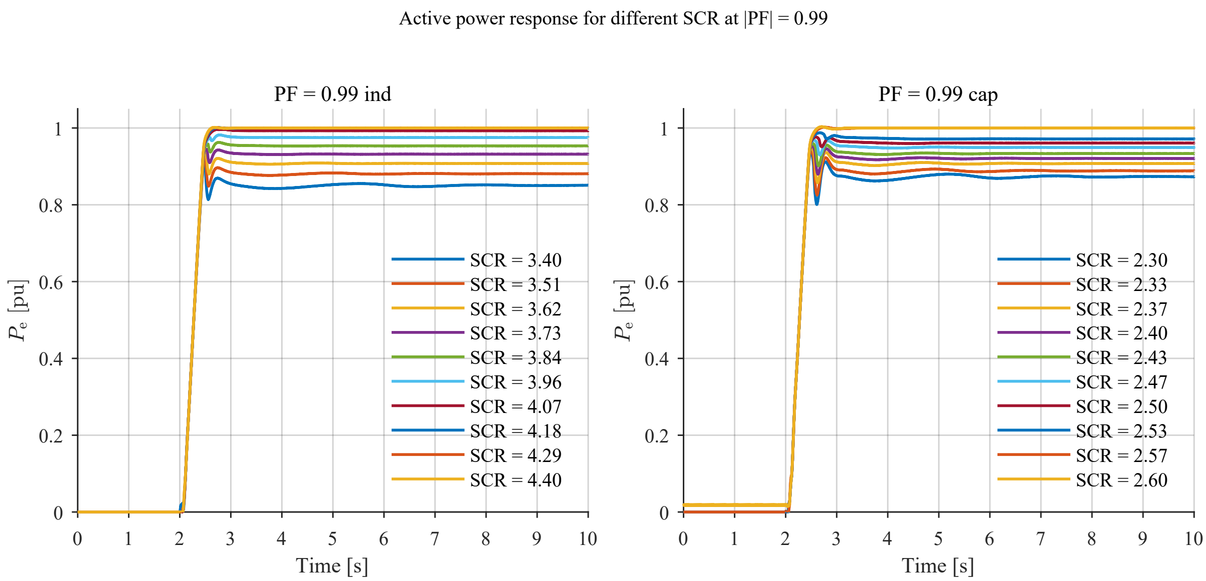

Figure 27: Active-power response under constant power factor for $|PF| = 0.99$, comparing inductive and capacitive operation for different SCR values.

Overall, the capacitive cases are able to operate at lower SCR values than the corresponding inductive cases. This is consistent with the weak-grid interpretation: capacitive operation injects reactive power and supports the PCC voltage, whereas inductive operation absorbs reactive power and increases the voltage drop across the grid impedance. Nevertheless, even when the theoretical power-angle limit is not binding, the active-power response can still fall below 1 pu because the converters must allocate current to satisfy the imposed reactive-power condition and the available current margin for active-power transfer is reduced.

References

[1] P. Fernández-Bustamante, O. Barambones, I. Calvo, C. Napole, and M. Derbeli, "Provision of frequency response from wind farms: A review," *Energies*, vol. 14, no. 20, p. 6689, 2021.

[2] H. Wang, H. He, Z. Yang, G. Li, Z. Chen, J. Yang, G. Zhang, and H. Dong, "Frequency response methods for grid-connected wind power generations: A review," *Electric Power Systems Research*, vol. 221, p. 109396, 2023.

[3] J. Boyle and T. Littler, "A review of frequency-control techniques for wind power stations to enable higher penetration of renewables onto the irish power system," *Energy Reports*, vol. 12, pp. 5567–5581, 2024.

[4] L. Li, D. Zhu, X. Zou, J. Hu, Y. Kang, and J. M. Guerrero, "Review of frequency regulation requirements for wind power plants in international grid codes," *Renewable and Sustainable Energy Reviews*, vol. 187, p. 113731, 2023.

[5] X. Guo, D. Zhu, X. Zou, Y. Yang, Y. Kang, W. Tang, and L. Peng, "Analysis and enhancement of active power transfer capability for DFIG-based WTs in very weak grid," *IEEE Journal of Emerging and Selected Topics in Power Electronics*, vol. 10, no. 4, pp. 3895–3906, 2021.

[6] B. Lu, S. Li, H. S. Das, Y. Gao, J. Wang, and M. Baggu, "Dynamic P-Q capability and abnormal operation analysis of a wind turbine with doubly fed induction generator," *IEEE Journal of Emerging and Selected Topics in Power Electronics*, vol. 10, no. 4, pp. 4854–4864, 2021.

[7] E. Fedele, D. Lauria, and R. Rizzo, "DFIG capability under weak grid connection and different reactive power control modes," in *2023 International Conference on Clean Electrical Power (ICCEP)*. IEEE, 2023, pp. 896–902.

[8] A. Bubshait and M. G. Simões, "Optimal power reserve of a wind turbine system participating in primary frequency control," *Applied Sciences*, vol. 8, no. 11, p. 2022, 2018.

[9] J. Ouyang, M. Pang, M. Li, D. Zheng, T. Tang, and W. Wang, "Frequency control method based on the dynamic deloading of DFIGs for power systems with high-proportion wind energy," *International Journal of Electrical Power & Energy Systems*, vol. 128, p. 106764, 2021.

[10] X. Du and J. Yu, "A singular spectrum analysis and gaussian process regression-based prediction method for wind power frequency regulation potential," *Energies*, vol. 15, no. 14, p. 5126, 2022.

[11] C. Yan, Y. Tang, J. Dai, C. Wang, and S. Wu, "Uncertainty modeling of wind power frequency regulation potential considering distributed characteristics of forecast errors," *Protection and Control of Modern Power Systems*, vol. 6, no. 3, pp. 1–13, 2021.

[12] S. Tian, Y. Liu, X. Tian, B. Li, and Y. Chi, "A wind farm control strategy for frequency regulation reserve: Optimize wake loss and frequency support capability," *Renewable Energy*, vol. 237, p. 121645, 2024.

[13] C. Pan, C. Shao, B. Hu, K. Xie, C. Li, and J. Ding, "Modeling the reserve capacity of wind power and the inherent decision-dependent uncertainty in the power system economic dispatch," *IEEE Transactions on Power Systems*, vol. 38, no. 5, pp. 4404–4417, 2022.

[14] Y. Zhang, S. Wu, J. Lin, Q. Wu, C. Shen, and F. Liu, "Frequency reserve allocation of large-scale res considering decision-dependent uncertainties," *IEEE Transactions on Sustainable Energy*, vol. 15, no. 1, pp. 339–354, 2023.

[15] T. Soares, P. Pinson, T. V. Jensen, and H. Morais, "Optimal offering strategies for wind power in energy and primary reserve markets," *IEEE Transactions on Sustainable Energy*, vol. 7, no. 3, pp. 1036–1045, 2016.

[16] T. Soares, P. Pinson, and H. Morais, "Wind offering in energy and reserve markets," in *Journal of Physics: Conference Series*, vol. 749, no. 1. IOP Publishing, 2016, p. 012021.

[17] J. Liang, S. Grijalva, and R. G. Harley, "Increased wind revenue and system security by trading wind power in energy and regulation reserve markets," *IEEE Transactions on Sustainable Energy*, vol. 2, no. 3, pp. 340–347, 2011.

[18] C. Edmunds, S. Martín-Martínez, J. Browell, E. Gómez-Lázaro, and S. Galloway, "On the participation of wind energy in response and reserve markets in great britain and spain," *Renewable and Sustainable Energy Reviews*, vol. 115, p. 109360, 2019.

[19] X.-Y. Yang, Y.-X. Liu, and G.-T. Xing, "Analysis of wind farm participation in the frequency regulation market considering wind power uncertainty," *International Journal of Electrical Power & Energy Systems*, vol. 130, p. 106946, 2021.

[20] T. Soares, T. V. Jensen, N. Mazzi, P. Pinson, and H. Morais, "Optimal offering and allocation policies for wind power in energy and reserve markets," *Wind Energy*, vol. 20, no. 11, pp. 1851–1870, 2017.

[21] S. A. Hosseini, J.-F. Toubeau, Z. De Grève, and F. Vallée, "An advanced day-ahead bidding strategy for wind power producers considering confidence level on the real-time reserve provision," *Applied Energy*, vol. 280, p. 115973, 2020.

[22] D. Cao, W. Hu, X. Xu, T. Dragičević, Q. Huang, Z. Liu, Z. Chen, and F. Blaabjerg, "Bidding strategy for trading wind energy and purchasing reserve of wind power producer: A DRL-based approach," *International Journal of Electrical Power & Energy Systems*, vol. 117, p. 105648, 2020.

[23] A. Stratman, W. Qiao, and L. Qu, "Optimal bidding strategy for a wind power producer in the energy and spinning reserve markets," in *2021 North American Power Symposium (NAPS)*. IEEE, 2021.

[24] S. A. Hosseini, J.-F. Toubeau, Z. De Grève, Y. Wang, N. Amjady, and F. Vallée, "Data-driven multi-resolution probabilistic energy and reserve bidding of wind power," *IEEE Transactions on Power Systems*, vol. 38, no. 1, pp. 85–99, 2023.

[25] X. Cheng, J. Lin, F. Liu, Y. Qiu, Y. Song, J. Li, and S. Wu, “A coordinated frequency regulation and bidding method for wind-electrolysis joint systems participating within ancillary services markets,” *IEEE Transactions on Sustainable Energy*, vol. 14, no. 3, pp. 1370–1384, 2022.

[26] B. Jiang, C. Guo, and Z. Chen, “Frequency constrained dispatch with energy reserve and virtual inertia from wind turbines,” *IEEE Transactions on Sustainable Energy*, vol. 16, no. 2, pp. 1340–1355, 2025.

[27] Y. Jiang and S. Zhao, “Market scheduling and pricing for comprehensive frequency regulation services,” *Journal of Modern Power Systems and Clean Energy*, vol. 13, no. 4, pp. 1407–1419, 2025.

[28] M. Mabboux-Fort, M. Bastankhah, P. C. Matthews, and M. Bozorg, “Optimal wind farm energy and reserve scheduling incorporating wake interactions,” *Applied Energy*, vol. 414, p. 127815, 2026.

[29] B. W. Tuinema, E. Adabi, P. K. Ayivor, V. García Suárez, L. Liu, A. Perilla, Z. Ahmad, J. L. Rueda Torres, M. A. van der Meijden, and P. Palensky, “Modelling of large-sized electrolysers for real-time simulation and study of the possibility of frequency support by electrolysers,” *IET Generation, Transmission & Distribution*, vol. 14, no. 10, pp. 1985–1992, 2020.

[30] X. Wang, D. W. Gao, J. Wang, W. Yan, W. Gao, E. Muljadi, and V. Gevorgian, “Implementations and evaluations of wind turbine inertial controls with fast and digital real-time simulations,” *IEEE Transactions on Energy Conversion*, vol. 33, no. 4, pp. 1805–1814, 2018.

[31] H. Shao, X. Cai, D. Zhou, Z. Li, D. Zheng, Y. Cao, Y. Wang, and F. Rao, “Equivalent modeling and comprehensive evaluation of inertia emulation control strategy for dfig wind turbine generator,” *IEEE Access*, vol. 7, pp. 64 798–64 811, 2019.

[32] M. Khoshjahan and M. Kezunovic, “Real-time simulator study of the n-grid ancillary service product delivery impact on the electric grid,” in *IEEE PES/IAS PowerAfrica Conference*, 2023.

[33] M. Kezunovic, M. Soleimani, H. Abu-Rub, S. Bayhan, and M. Trabelsi, “Hardware in the loop simulation of a nano-grid transactive energy exchange,” in *2019 2nd International Conference on Smart Grid and Renewable Energy (SGRE)*. IEEE, 2019, pp. 1–6.

[34] Y.-K. Chung and Y.-K. Wu, “Novel frequency control strategy by wind turbines considering wind speed fluctuations and optimized power point tracking,” *IEEE Transactions on Industry Applications*, 2024.

[35] L.-R. Chang-Chien, W.-T. Lin, and Y.-C. Yin, “Enhancing frequency response control by DFIGs in high wind-penetrated power systems,” *IEEE Transactions on Power Systems*, vol. 26, no. 2, pp. 710–718, 2010.

[36] I. D. Margaris, S. A. Papathanassiou, N. D. Hatziargyriou, A. D. Hansen, and P. Sørensen, “Frequency control in autonomous power systems with high wind power penetration,” *IEEE Transactions on Sustainable Energy*, vol. 3, no. 2, pp. 189–199, 2012.

[37] G. C. Tarnowski, P. C. Kjær, S. Dalsgaard, and A. Nyborg, “Regulation and frequency response service capability of modern wind power plants,” in *IEEE PES General Meeting*. IEEE, 2010, pp. 1–8.

[38] Fingrid Oyj, "FCR: Frequency containment reserves," Online, 2026, accessed: 2026-06-05. [Online]. Available: https://www.fingrid.fi/en/electricity-market/reserves/reserve-products/frequency-containment-reserves-fcr-products/

[39] ——, "Appendix 2: The technical requirements and the prequalification process of frequency containment reserves (FCR)," Fingrid Oyj, Tech. Rep., 2025. [Online]. Available: https://www.fingrid.fi/globalassets/dokumentit/fi/sahkomarkkinat/reservit/appendix-2-the-technical-requirements-and-the-prequalification-process-of-frequency-containment-reserves-fcr.pdf

[40] ——, "Dataset 315: Hourly volume of procured frequency containment reserve for disturbances upwards regulation (FCR-D Up)," Fingrid Open Data, 2026, accessed: 2026-06-05. [Online]. Available: https://data.fingrid.fi/en/datasets/315

[41] ——, "Dataset 318: Frequency containment reserve for disturbances upwards regulation, hourly market price," Fingrid Open Data, 2026, accessed: 2026-06-05. [Online]. Available: https://data.fingrid.fi/en/datasets/318

[42] A. Boričić, J. L. R. Torres, and M. Popov, "System strength: Classification, evaluation methods, and emerging challenges in IBR-dominated grids," in *2022 IEEE PES Innovative Smart Grid Technologies–Asia (ISGT Asia)*. IEEE, 2022, pp. 185–189.

[43] CIGRE Working Group B4.62, "Connection of wind farms to weak AC networks," CIGRE, Technical Brochure 671, 2016. [Online]. Available: https://www.e-cigre.org/publications/detail/671-connection-of-wind-farms-to-weak-ac-networks.html

[44] C. Guo and D. Wang, "Frequency regulation and coordinated control for complex wind power systems," *Complexity*, vol. 2019, p. 8525397, 2019.

[45] J. Zhang and J. Li, "Hybrid deloading control strategy in MMC-based wind energy conversion systems for enhanced frequency regulation," *Energies*, vol. 17, no. 5, p. 1253, 2024.

[46] ENTSO-E, "Transparency Platform: Energy Prices [12.1.D], Finnish bidding zone," https://transparency.entsoe.eu/market/energyPrices, 2026, day-ahead electricity prices for Finland bidding zone BZN|10YFI-1———U, March 2026. Accessed: 2026-06-08.

[47] Fingrid Oyj, "Terms and conditions for providers of frequency containment reserves (FCR)," Online, May 2024, accessed: 2026-06-08. [Online]. Available: https://www.fingrid.fi/globalassets/dokumentit/en/electricity-market/reserves/terms-and-conditions-for-providers-of-frequency-containment-reserves-fcr-id-391152.pdf

[48] Comisión Nacional de Energía, "Norma técnica de seguridad y calidad del servicio: Anexo técnico de metodología para el estudio de análisis de robustez del sistema eléctrico nacional," Comisión Nacional de Energía, Santiago, Chile, Tech. Rep., Jan. 2026.